SEDIMENTOLOGY the journal of the International Association of Sedimentologists

Sedimentology (2017) doi: 10.1111/sed.12375

Interpreting flash flood palaeoflow parameters from antidunes and gravel lenses: An example from Montserrat, West Indies

MELANIE J. FROUDE*†, JAN ALEXANDER*, JENNI BARCLAY* and PAUL COLE‡
**School of Environmental Sciences, University of East Anglia, Norwich Research Park, Norwich, Norfolk NR4 7TJ, UK (E-mail: m.froude@sheffield.ac.uk)*
†Department of Geography, University of Sheffield, 9 Northumberland Road, Sheffield S10, UK
‡Earth Sciences, Plymouth University, Drake Circus, Plymouth, Devon PL4 8A, UK

Associate Editor – Vern Manville

ABSTRACT

The wavelength of stationary water-surface waves and their associated antidune bedforms are related to the mean velocity and depth of formative flow. In past published sand-bed flume experiments, it was found that lens structures were preserved during antidune growth and change, and the dimension of the lenses was empirically related to antidune wavelength, and thus could be used to estimate flow velocity and depth. This study is the first to compare observations of formative flow conditions and resulting sedimentary structures in a natural setting, testing the previously published relationship at a field-scale. Trains of stationary and upstream migrating water-surface waves were prevalent during the flash flood in October 2012 in the Belham Valley, Montserrat, West Indies. Wave positions and wavelengths were assessed at 900 sec intervals through the daylight hours of the event within a monitored reach. The wave data indicate flow depths up to 1·3 m and velocity up to 3·6 m sec^{-1}. Sedimentary structures formed by antidune growth and change were preserved in the event deposit. These structures include lenses of clast-supported gravel and massive sand, with varying internal architecture. The lenses and associated low-angle strata are comparable to sand-bed structures formed from stationary and upstream migrating waves in flume experiments, confirming the diagnostic value of these structures. Using mean lens length in the event deposit underestimated peak flow conditions during the flood and implied that the lenses were preserved during waning flow.

Keywords Antidunes, flash flood, gravel lenses, lahar, palaeoflow.

INTRODUCTION

Sedimentary structures associated with supercritical flow conditions are very poorly documented in comparison with structures produced in subcritical flow conditions and, consequently, are still rarely recognized in the rock record. (Maejima *et al.*, 2009). It is very difficult, both technically and because of inherent hazards, to observe sedimentary processes in natural supercritical flows above mobile beds directly because of the fast, turbulent, sediment-laden water. Sedimentary structures resulting from formation, migration and truncation of antidunes have been documented in sand-bed flumes with and without bed aggradation (e.g. Alexander *et al.*, 2001; Yokokawa *et al.*, 2010), but there are no published studies in natural settings that compare the formative flow conditions and the resulting sedimentary structures. Alexander *et al.* (2001) suggested that the dimensions of lenses formed in flumes under stationary water-surface waves are related to antidune wavelength and thus could be used to estimate flow velocity and

depth (Fig. 1). The Alexander *et al.* (2001) empirical relationship was used by Duller *et al.* (2008) to infer flow conditions in the 1918 Katla jökulhlaup from lenses preserved in sand-granule grade deposits. While this demonstrated the utility of the relationship to palaeoflow reconstruction, there were no direct measurements of the flow conditions which generated the documented deposit.

This article presents a unique data set that reinforces the field applicability of empirical relationships to the study of sedimentary structures generated by supercritical flow. Measurements of water-surface waves in a flash flood and lenses in the gravel deposits of the same flood within a study reach are compared to test the Alexander *et al.* (2001) relationship for lens size as an indicator of flow conditions, for the first time on a field-scale example. These measurements are compared to flow velocities derived from flow competency relationships using the dimensions of clasts observed in transport in the flood, and boulders in the event deposit.

Deposit grain size has been used to indicate palaeoflow velocity (e.g. Costa, 1983; Komar, 1987; Clarke, 1996; Mather & Hartley, 2005), but this is beset with problems associated with accounting for form drag, emergence, grain packing, sorting and exposure, suspended sediment concentration, slope and flow unsteadiness (Laronne & Carson, 1976; Church, 1978; Andrews, 1983; Church *et al.*, 1998; Meirovich *et al.*, 1998; Shvidchenko & Pender, 2000; Carling *et al.*, 2002a,b; Petit *et al.*, 2005; Billi, 2011; Parker *et al.*, 2011; Alexander & Cooker, 2016). Importantly, the sizes of sediment available for transport impacts the reliability of grain size as a palaeoflow indicator. This study provides a test for the usefulness of antidune lens size as an alternative indicator of depositional flow conditions. The diagnostic value of lens size for flow conditions may be more reliable in conditions where flow is fully turbulent, rapidly varying, unsteady and Newtonian. This is often the case in flash floods: flows have the competence to transport larger clasts than are available for

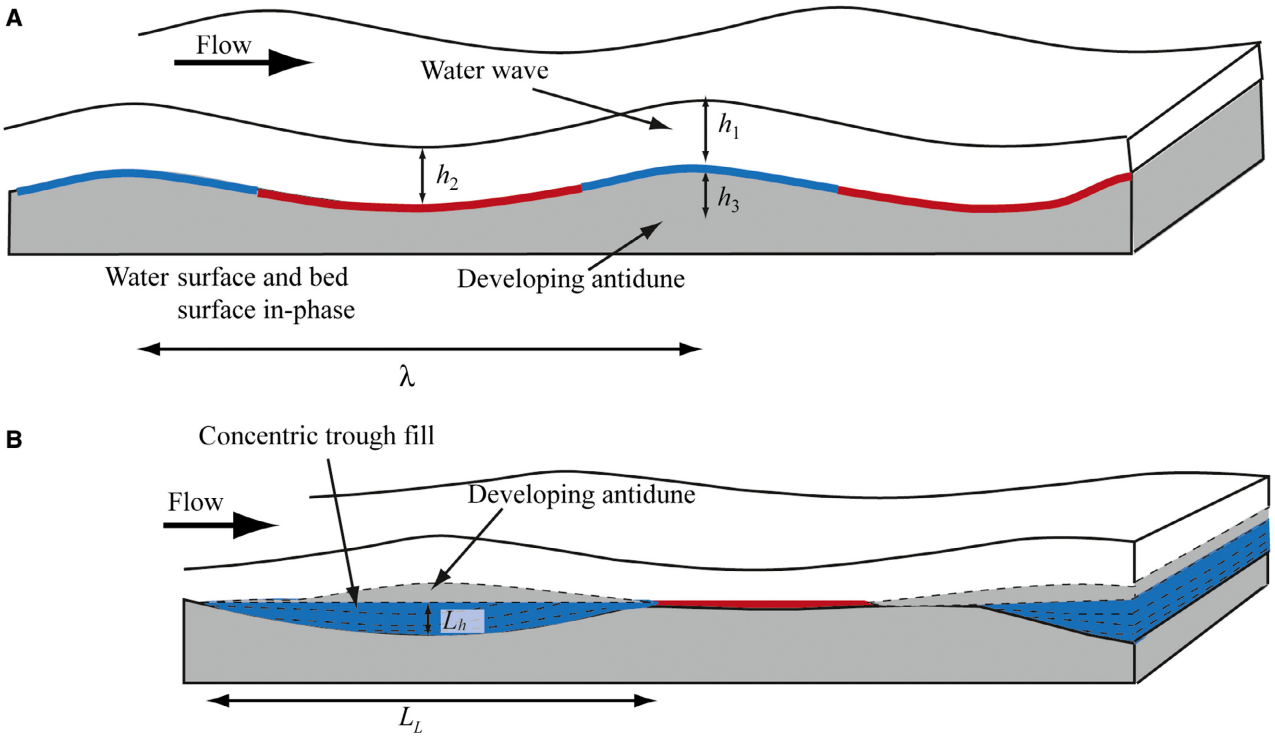

Fig. 1. (A) The geometries of a two-dimensional water-surface wave and antidune. Water-surface wave (and antidune) wavelength, λ, water wave depth (h_1), water depth at the trough (h_2), antidune height (h_3). Areas of erosion (red) and deposition (blue) shown corresponding to accelerating or decelerating flow, respectively. (B) Sediment is deposited in the eroded trough [in (A)] during wave breaking and upstream migration of the antidune. The preserved lenticular length, L_l, and lenticular thickness, L_h, is shown to be smaller than the original antidune wavelength and height.

transport. In these situations, maximum clast size would underestimate palaeoflow velocity. Antidune wavelength is independent of grain size, so lens length could generate more reliable estimates, and using both methods provides more information and thus confidence to interpretations.

Water-surface waves and antidunes

Stationary water-surface waves are often observed in rivers and floods when flow velocity is greater than or equal to the celerity of water-surface waves, i.e. when the Froude number, *Fr*, is equal to or greater than 1 ($Fr = U/(gh)^{0.5}$, where U is mean velocity, h is flow depth, and g is acceleration due to gravity). In these flow conditions, over a non-cohesive mobile bed, feedback between the flow and the bed will form sediment waves (antidunes) that are in-phase with, or nearly in-phase with, the water-surface waves (Fig. 1). The wave crests of stationary water-surface waves remain in fixed positions or move slowly upstream or downstream (Núñez-González & Martín-Vide, 2011). It is important to differentiate these waves from a standing wave, which in the strict sense is a stationary wave which oscillates about a fixed point (node) at a frequency relative to the confining conditions; waves related to antidunes do not oscillate in this way.

Supercritical or near-critical flows that contain moving gravel make the collection of precise velocity data particularly difficult. Measuring depth precisely in fast flows over non-cohesive mobile beds is also challenging. However, it is possible to estimate flow conditions from water-surface wave dimensions (Tinkler, 1997a,b; Douxchamps *et al.*, 2005) and this approach is used herein. Kennedy (1963) defined relationships between the wavelength, λ, of stationary water-surface waves and mean flow velocity, U, for two-dimensional waves (where the crest-parallel length is long compared to the wavelength):

$$U = \sqrt{\left(\frac{g\lambda}{2\pi}\right)} \tag{1}$$

and between λ and the mean flow depth, h_m:

$$h_m = \frac{\lambda}{2\pi} \tag{2}$$

where two stationary water-surface wave trains interact at an angle (due to bed or bank topography), the resulting waves may have short crests and are thus called 'three-dimensional waves' (Yokokawa *et al.*, 2010) or colloquially 'rooster tails' (Kennedy, 1961). Kennedy's (1961) Eq. 1 modified for three-dimensional waves is:

$$U = \sqrt{\frac{g\lambda}{2\pi}} \cdot \left[1 + \left(\frac{\lambda}{\lambda_t}\right)^2\right]^{\frac{1}{4}} \tag{3}$$

where λ_t is the transverse wavelength of the waveform.

Antidune bedforms develop in-phase or intermittently in-phase (with breaking waves) with the water-surface waves and have the same wavelength (Allen, 1982), which is controlled by the water depth and velocity and thus largely independent of the bed composition (grain size) (*cf.* Cartigny *et al.*, 2014). Consequently, preserved antidunes can be used to estimate palaeoflow depth and velocity (e.g. Kennedy, 1963; Barwis & Hayes, 1985; Alexander & Fielding, 1997; Fralick, 1999; Carling *et al.*, 2009). Antidune wavelength is considered a more reliable palaeoflow indicator than dune size (Vesipa *et al.*, 2014).

Trains of stationary water-surface waves have been observed in many settings where fast shallow flow occurs, including, for example, glacier outburst floods (Magnússon *et al.*, 2012; see video clip at youtube.com/watch?v=9sryalI57oo), rain-storm induced flash floods in arid and semi-arid settings (Reid & Frostick, 1987; Jones & Mulholland, 1999), rockbed and gravel-bed channels (Tinkler, 1997a,b), sand-bed channels on beaches (Grant, 1997) and in lahars (Pierson & Scott, 1985; Hayes *et al.*, 2002). The prevalence of water-surface waves in certain environments highlights the potential of antidune deposits for palaeoflow reconstruction, if sedimentary structures associated with antidunes are preserved and identified in the sediment record.

Sedimentary structures resulting from antidune formation, migration and truncation

Flume-generated antidunes are well-documented (Jopling & Richardson, 1966; Yagishita & Taira, 1989; Alexander *et al.*, 2001; Yokokawa *et al.*, 2010; Carling *et al.*, 2014), and antidunes have been described from a wide range of modern settings including rivers (e.g. Harms & Fahnestock, 1965; Shaw & Kellerhals, 1977; Langford & Bracken, 1987; Cotter & Graham, 1991; Alexander & Fielding, 1997), alluvial fans (e.g. Blair & McPherson, 1999; Blair, 2000), washover fans

(Barwis & Hayes, 1985), glacial outwash streams (e.g. Fralick, 1999; Kjaer *et al.*, 2004), glacial outburst floods (e.g. Burke *et al.*, 2010; Lang & Winesmann, 2013), jökulhlaups triggered by volcanic activity (e.g. Duller *et al.*, 2008; Marren *et al.*, 2009), tsunami run-up deposits (e.g. Fujiwara & Tanigawa, 2014) and also in the rock record (e.g. Browne & Plint, 1994; Maejima *et al.*, 2009). In most settings, the morphology of the original antidune is rarely preserved sufficiently well to measure wavelength (Alexander & Fielding, 1997; Fielding, 2006). The sedimentary structures resulting from formation, migration and truncation of antidunes are more likely to be preserved than the topographic form of antidunes on a bed. These structures are increasingly well-understood and recognizable (*cf.* Alexander *et al.*, 2001 and Duller *et al.*, 2008).

Combining the flume observations of Middleton (1965), McBride *et al.* (1975), Foley (1977), Yagishita & Taira (1989), Yokokawa *et al.* (1999), Alexander *et al.* (2001), Breakspear (2008), Yokokawa *et al.* (2010) and Cartigny *et al.* (2014) provides a scheme of reference for field interpretation of the sedimentary architecture of antidune deposits (Table 1; Fig. 2). Different modes of water-surface wave breaking have been associated with different sedimentary structures. Cartigny *et al.* (2014) demonstrated that 'stable antidunes' (non-breaking waves) produced upstream-dipping laminae sets; the thickness and internal architecture depending on factors including bed aggradation rate. 'Unstable antidunes' (formed under breaking waves) produce lenses with a variety of internal fabric and lamination depending on wave behaviour. Sand lenses with boundary-conformable laminae are characteristic of 'unstable antidunes' (Middleton, 1965; Hand, 1974; Alexander *et al.*, 2001; Duller *et al.*, 2008; Cartigny *et al.*, 2014). Gravel lenses with comparable internal architectures to such sand lenses were observed by Breakspear (2008).

THE BELHAM RIVER ON THE ISLAND OF MONTSERRAT, WEST INDIES

The Soufrière Hills volcano on the island of Montserrat (16·72°N, 62·18°W, Fig. 3A and B) has been in episodic eruption since July 1995 (Wadge *et al.*, 2014). Eruptive products (pyroclastic density currents, lahars, debris avalanches and tephra-fall) from the lava dome have been deposited across the southern half of the island. The copious volumes of unconsolidated pyroclastic debris are being remobilized, transported and redeposited by frequent flash floods (lahars; Barclay *et al.*, 2007; Alexander *et al.*, 2010). Flash floods result from high intensity rainfall (more than 500 mm of rain often falls in a single event at intensities $\geq$50 mm h^{-1}) from localized and convective storms, and less frequent large-scale synoptic weather systems including hurricanes (Gray, 1979; Matthews *et al.*, 2002). The magnitude of flash flooding has increased in response to catchment changes, resulting directly and indirectly from volcanic activity (Alexander *et al.*, 2010; Froude, 2015).

The Belham River Valley is located on the north-western flanks of the Soufrière Hills volcano (Fig. 3C). Pre-1995, the whole catchment was densely vegetated with areas of dry (29%), mesic (48%) and wet forest (13%) (Young, 2008; Fig. 4A to C) and small-scale agricultural production. Since July 1995, volcanic activity has damaged or destroyed large areas of vegetation, resulting in bare earth surfaces and a predominance of dry forest species on revegetating slopes. Extensive volcanic deposits and the changes in vegetation have profoundly altered run-off dynamics (Alexander *et al.*, 2010; Froude, 2015). Between July 1995 and March 2013, $5{\cdot}1 \times 10^7$ m^3 (estimated from repeat topographic survey; Froude, 2015) of volcanic sediment was deposited on the Belham Catchment. Flash floods remobilized more than 10×10^6 m^3 of this primary volcanic material into the Belham Valley with an estimated $4{\cdot}4 \times 10^6$ m^3 remaining in channel storage and the rest transported offshore (Froude, 2015).

Volcanic activity, increases in flash flooding magnitude and frequency, and increased sediment flux have transformed the morphology of the Belham River from its former narrow (2 to 3 m) gravel-bed channel, confined by steep valley sides (Fig. 4D and H). The valley floor has aggraded by an average of 9·45 m (maximum 31·11 m; Fig. 5) and steepened. From the Sappit River confluence to point E on Fig. 3C, the gradient of the Belham Valley has increased from 0·8° to 2·86°. Due to aggradation, the channel width has increased from *ca* 2 m to between 59 m and 182 m (Froude, 2015). Local aggradation rates vary between successive flash floods and local incision also occurs, where steep-sided channels are cut and filled in successive

Table 1. Experimental conditions of published flume studies: observed sedimentary structures are shown in Fig. 2.

Study	Experimental conditions						Sedimentary structures (reference Fig. 2)
	Median grain size (D50) and SD in brackets	Froude number	Bedform wavelength (m)	Bedform amplitude (m)	Bedform migration	Bedform dimensionality	
Middleton (1965)	0·19 mm (1·44)	1·1–1·7	1·0–2·0	0·05	Upstream	2D	1–6, 8, 16
McBride *et al.* (1975) Runs 7/12 and 6/12	0·34 mm and 0·50 mm (0·71 and 1·26)	1·4 and 1·0	0·1–0·2	0·02–0·08	Downstream	2D	16
Foley (1977)	μ = 0·28 mm (1·42)	1·37	0·4	0·06	Stationary	3D	8, 12
Yagishita & Taira (1989)	μ = 0·5 mm (1·42)	1·66–1·76	0·6–0·7	0·03	Upstream	2D	8, 17
Yokokawa *et al.* (1999)	0·18 mm	1·3	0·4–1·0	0·01–0·02	Upstream	2D	5–6, 8–9, 11–13
Alexander *et al.* (2001)	0·42 mm (0·71)	1·5–1·71	0·76–1·14	0·035–0·066	Stationary – upstream	2D	3, 6–11, 13–16
Breakspear (2008) A, Run 1	1·21 mm (1·49)	1·59	0·4	0·02	Upstream	3D	1, 5, 8–9. 12–15, 18
Breakspear (2008) B, Run 2	1·06 mm (1·32)	1·35-1·75	0·44	0·018	Upstream	2D/3D	2, 5, 12–13, 19, 22
Yokokawa *et al.* (2010)	0·18 mm (0·44)	1·26–2·62	0·4–0·5	0·015–0·02	Stationary –upstream	2D and 3D	2–3, 5–11, 14–16
Cartigny *et al.* (2014) A, synthetic aggradation technique Stable antidunes Runs [7, 11], [18-19, 22]	0·35 mm and 0·265 mm	Fr50 = 1·0–1·41	–	–	Upstream	2D	7, 18–19
Cartigny *et al.* (2014) B, synthetic aggradation technique Unstable antidunes Run 3	0·16 mm	Fr50 = 1·07	–	–	Upstream	2D	3, 8, 10, 14, 20–21

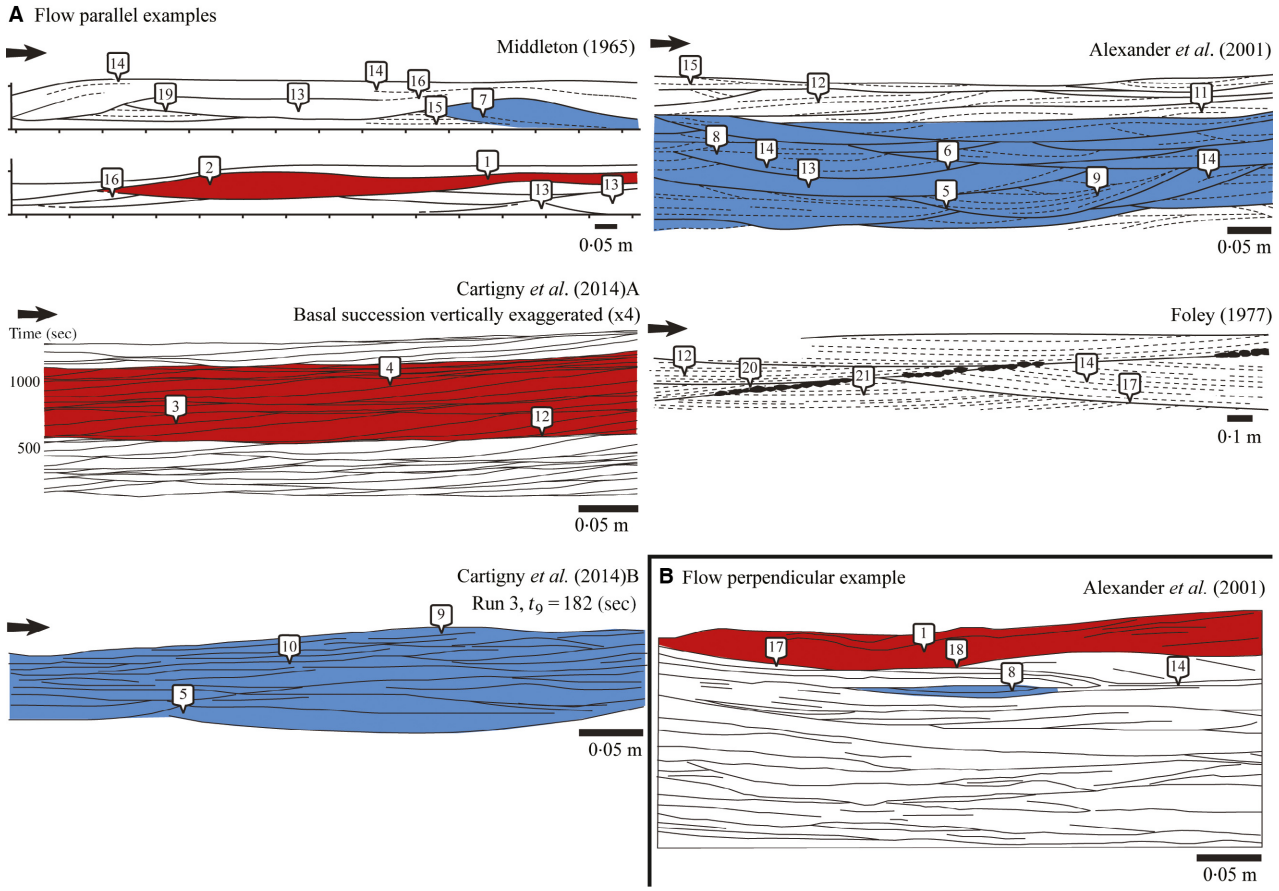

Fig. 2. A scheme of reference for field interpretation of sedimentary structures resulting from antidunes, combining published flume observations [flow-parallel sections in (A) and flow perpendicular in (B)]. The experimental conditions of each study are provided in Table 1 (note that in Cartigny *et al.*, 2014, structures were generated by the synthetic aggradation method). Tabular bedset (red): [1] tabular bedset, pinches/swells laterally; [2] tabular bedset with faint bedding; [3] tabular beddset with low-angle backset laminae; [4] lamina thickness decreases upwards within lamina set. Lenticular bedset (blue): [5] truncation of lenticular sets; [6] superimposed trough sets; [7] lenticular bedset containing low-angle downstream dipping laminae; [8] lenticular laminae sets with concave upward erosional surfaces; [9] lenticular bedset containing low-angle upstream-dipping laminae; [10] lenticular sets that are structureless at the base and grade vertically to more stratified deposit. Laminae: [11] convex-upward laminae; [12] upstream-dipping laminae that downlap onto the basal surface asymptotically; [13] visually structureless laminae; [14] parallel lamination discontinuous; [15] planar, parallel lamination. Bedset boundary: [16] laterally discontinuous basal surface or bounding surface; [17] stratification sub-parallel to basal bedset surface; [18] gradational boundary between lenticular set and tabular set; [19] downstream dipping erosional surfaces. Other: [20] gravel lag/dropout armour; [21] remnant basal bedset.

events (Fig. 4F and I). The Belham River is ephemeral, and for most of the year the valley floor is dry; flash flooding occurs for short periods after rain storms. Flow is highly unsteady, intensely turbulent and sediment-laden (Barclay *et al.*, 2007; Alexander *et al.*, 2010). Stationary waves are prevalent in the middle and lower reaches of the river during all observed flow events.

The sediment deposited during 2009 to 2013 in the Belham Valley ranges from clay-grade (volcanic ash) to boulders (up to and greater than 2 m diameter). The valley floor varies in space and time from boulder fields (Fig. 4E) to nearly flat sand sheets with primary current lineation (Fig. 4H) to mud draped surfaces (Fig. 4I). The thickest mud drapes form where flood water is locally and temporarily dammed (Fig. 4J). The bed has been repeatedly surveyed and sampled over the past two decades, and deposits examined where they are exposed in natural channel banks or artificial trench walls (Fig. 4K).

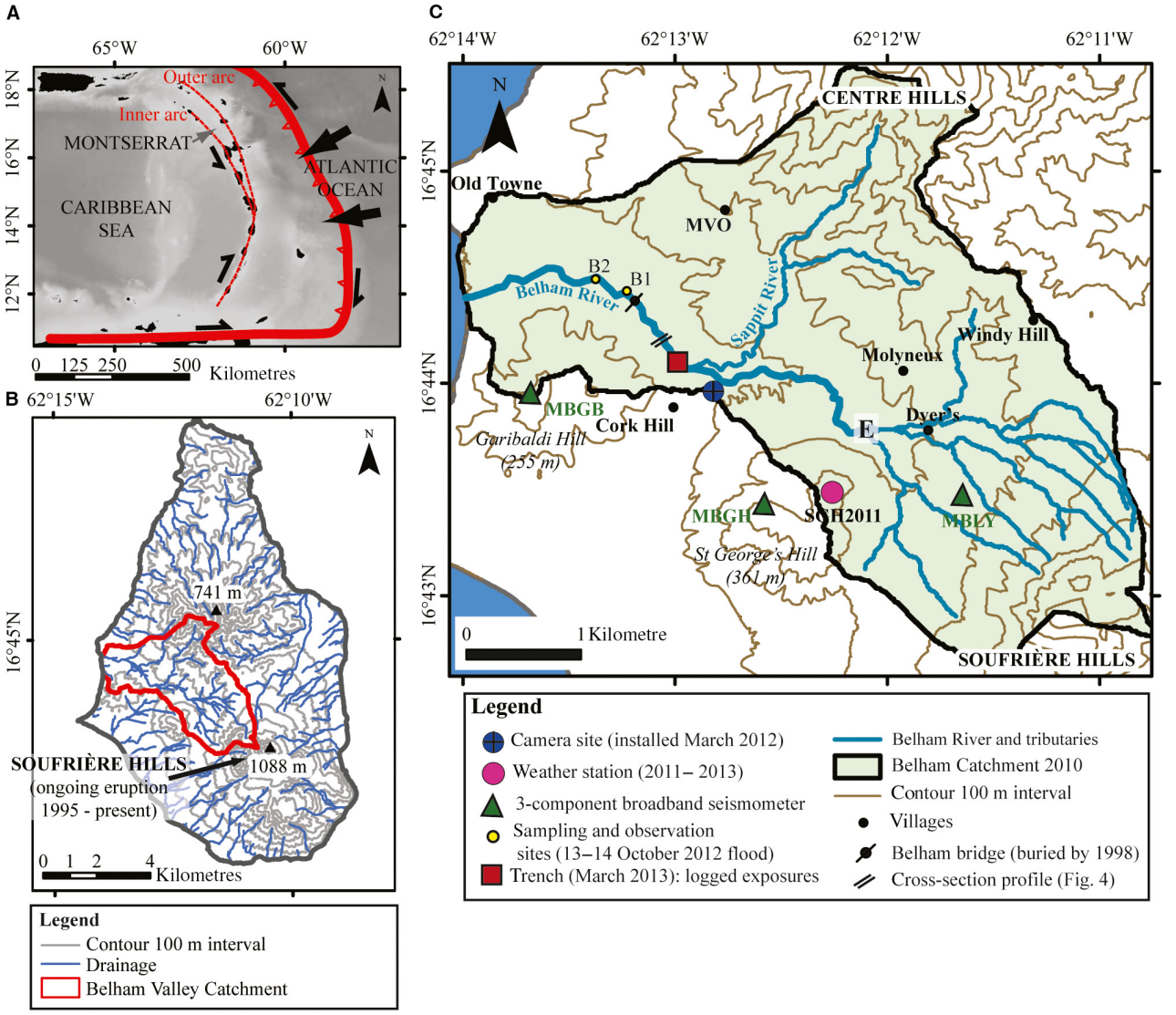

Fig. 3. (A) The location of Montserrat in the Lesser Antilles arc. Modified from Kenedi *et al.* (2010) and Cassidy *et al.* (2012). Base map: GEBCO bathymetry data (GEBCO, 2014). (B) Map of Montserrat showing the location of the Belham Catchment and the volcanic Soufrière Hills. Topographic base map: merged digital elevation model (DEM) from 1999 (north island) and 2010 (south of the island). (C) Map of the main drainage routes within the Belham Catchment and the locations of the monitoring camera (installed in March 2012), weather stations, seismometers, rain gauges, and sampling and observation sites. The catchment boundaries, drainage routes and contours were calculated from a digital elevation model (2010 topography).

METHODS

This study compares flow conditions during a sediment-laden flash flood with palaeoflow reconstructions using antidune lenses and grain size in the event deposit. To overcome the challenges inherent in observing sediment-laden flash floods, a camera was installed in a remote site overlooking a reach in the Belham River Valley. Imagery from this monitoring camera was used to measure flow properties (water-surface waves, boulders in transport and channel dimensions) during a flash flood event on 13 to 14 October 2012. Deposits of this event (before significant reworking) were examined on the dry bed and in trenches within 400 m of the camera site. Sedimentary structures developed in gravel that are comparable to the flume sand structures are documented, confirming their diagnostic application. Data on stationary waves in the flash flood and gravel lens architecture in the event's deposits are used to test the flume-

Fig. 4. Sites of interest in the Belham River Valley. Foreground scale of the photograph included, unless otherwise stated in figure caption. (A) Dry Forest. (B) Mesic Forest. (C) Wet Forest. (D) The lower Belham River Valley pre-eruption, looking towards the Soufrière Hills (photograph reproduced with permission, Richard Herd). Field of view (12·5° horizontal, 5° vertical). (E) Looking upstream from 100 m upstream of B1 (Fig. 3C), April 2000. The bed surface was covered with 0·5 to 1·0 m boulders that were resting (not buried) on a sand bed. Wood debris was also scattered across the valley floor. (F) Looking upstream from 300 m upstream of B1 (Fig. 3C). A large flash flood on 2 May 2006 incised 2 m into the valley floor (Sušnik, 2009). The two-storey orange house was gradually buried by lahar deposits between 2002 and 2010 (Froude, 2015). The incised channel width is 22 m. (G) Looking upstream towards the trench site (Fig. 3C), March 2012. The bed surface was *ca* 40% gravel: 60% sand with cobble-boulder bars in the centre of the valley and sand-pebble bars in the centre of sandy channels (*ca* 15 m wide) (Froude, 2015). Gravel bars remained unmodified in their central parts between November 2010 and March 2012. Vegetation growing within the channel indicates minimal disturbance. (H) Looking downstream and southward from site B2 (Fig. 3C) on 5 May 2011, immediately following a small flash flood. The half-buried house in the background (edge of valley floor) is *ca* 10 m wide. (I) Looking upstream and southward from 200 m downstream of site B2 (Fig. 3C) on 27 May 2011, immediately following a small flash flood. The half-buried house to the top right of the photograph is same as in (H). The flow had incised into a gravel bar in the centre of the valley floor, and deposited mud drapes over the bed surface down the entire valley floor. Some of the mud drapes have been removed by subsequent low-level flow. (J) Flow on 27 May 2011 pooled in commercial aggregate mining trenches (between site B1 and B2, Fig. 3C), leaving mud drapes. The trench width was *ca* 20 m, length *ca* 100 m and water depth <0·5 m. (K) Vertical exposure (the north side of the valley at B2, Fig. 3C) created by commercial aggregate extraction. Photograph from March 2011. Person is 1·57 m tall.

derived empirical relationship between antidune lens length and flow conditions (Alexander *et al.*, 2001).

Seismic flow monitoring

Flow is not directly gauged, but three-component seismometers, installed as part of the volcano monitoring network (Fig. 3C), continuously record the ground movements, and some of these movements are generated by flood events. The character of the seismic signal is used by the Montserrat Volcanic Observatory to monitor the occurrence and relative magnitude of flash floods, based on signal duration and number of peaks. Flash floods are identified as very long period (*ca* 10 min to several hours) seismic signals (Zobin *et al.*, 2009) that have an elevated 2 to 5 Hz signal and peaks between 1 Hz and 30 Hz, and are accompanied by seismic noise in the lower frequencies (<1 Hz). Elevated seismicity corresponds to increased turbulence, flow volume or sediment load (Doyle *et al.*, 2011). Seismic data thereby not only show the onset and duration of a flood, but also indicate peaks in discharge during an event. Signals interpreted as flash floods were verified by correlation with records of visual observation of the flood and

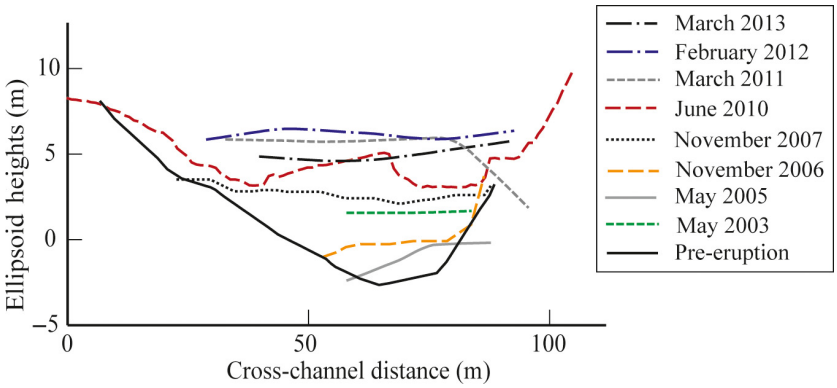

Fig. 5. Cross-section profile of a transect 100 m downstream of the trench site (Fig. 3C) showing elevation change due to primary volcanic and flash flood activity between July 1995 and March 2013 (Froude, 2015). Elevation data: pre-eruption DEM (Wadge, 2000); May 2003 (dGPS survey; Barclay *et al.*, 2007); May 2005 (dGPS survey; Sušnik, 2009); November 2006 (dGPS survey; Darnell, 2010); November 2007 (dGPS survey; Darnell, 2010); June 2010 (Airborne LiDAR; SAC, 2011); March 2011 (dGPS survey; Froude, 2015); February 2012 (dGPS survey; Froude, 2015); March 2013 (dGPS survey; Froude, 2015). Locally elevations in this part of the valley varied by ±1 m between March 2011 and March 2013.

rainfall records (Froude, 2015). Since 1995, the monitoring network has detected >585 rainfall-triggered flash floods of which >351 events have been verified visually: most of the unverified events occurred during the hours of darkness.

Remote monitoring camera: image acquisition and processing

In-person direct visual observation of valley-wide flows was limited to sites >5 km from the volcanic edifice, and these areas were frequently modified by commercial aggregate extraction. To monitor a section of the natural channel, unaffected by aggregate extraction, a telemetered remote camera was installed 3·8 km from the volcano in March 2012, upstream of any likely sand quarrying activity. The field of view of the camera encompassed a 50 to 69 m wide, 113 m long reach of the Belham River (herein referred to as the camera site).

The equipment comprised of a Stardot™ SC 5 megapixel IP camera (StarDot Technologies, Buena Park, CA, USA) with a wide-varifocal auto iris lens, powered by two 100 watt solar panels charging two 12-volt car batteries. Image capture was controlled by a custom built Raspberry Pi™ field computer running a Python script which captured five megapixel images at a rate of one frame per second during daylight hours, storing each image on a local hard drive. The camera was telemetered to the Montserrat Volcano Observatory, facilitating two-way data transfer.

Objects moving within the flow and surface flow features were measured within a sample cross-section, constrained by permanent poles and boulders of precise known locations (Fig. 6A). Photograph coordinates for the poles and boulders were obtained using DigitizeIt™ software. One pixel distance between P1 and R1 (vector A; Fig. 6A) equated to 0·026 m horizontal ground distance. One point between P2 and P3 equated to 0·047 m horizontal ground distance. Considering the distance between the vertices P1 and P3, a linear equation was derived to calculate the change in pixel:metre ratio between the foreground and background of the channel cross-section:

$$y = 0{\cdot}00035x + 0{\cdot}026 \qquad (4)$$

where x is the pixel distance from vertex P1 along the vector P1 to P3, and y is a scaling coefficient to convert one pixel to metres. The

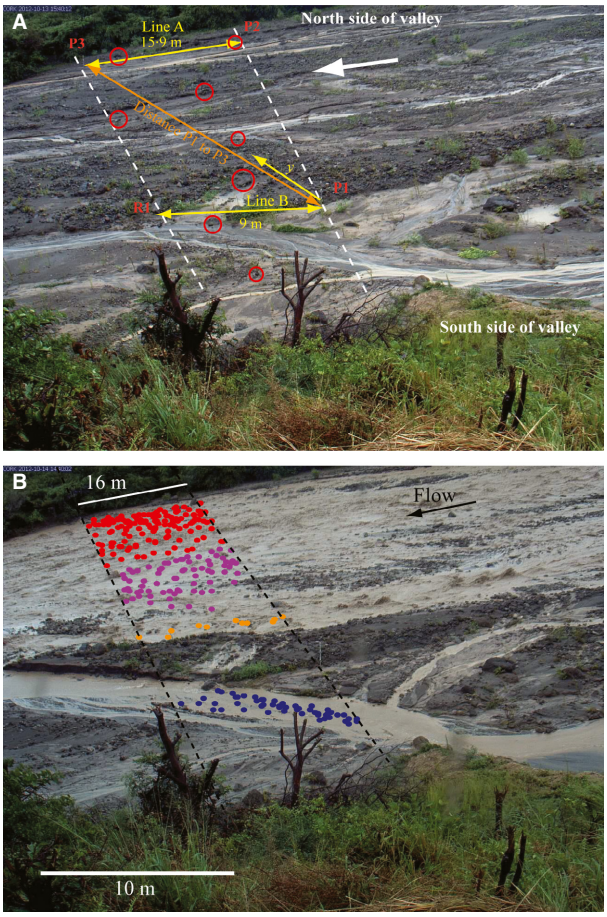

Fig. 6. (A) Locations of control points, P1, P2, P3 and rock (R1), on the valley floor at the camera site (Fig. 3C). Red circles are around objects of known size, used to validate Eq. 4. Multiple scale bars are included illustrating the change in scale between the foreground and background. (B) Location of sampled waves at the camera site. Waves are grouped by location, corresponding to the sub-channel structure on the valley floor. Sub-channels: north (red), north-middle (purple), south-middle (yellow), south (blue). The two north sub-channels coalesced during peak flow.

equation was tested using objects of known size spread across the sample cross-section (Fig. 6A). Error ranged from 0·1 m in the background of the image to 0·05 m in the foreground of the image.

Image coordinates for the crests of water-surface waves in wave trains were obtained using DigitizeIt™ software. The distance between image coordinates was calculated, and the location of the mid-point coordinate (equidistant between the two wave crests) was located on the P1 to P3 (vector, Fig. 6A), providing a value of x for Eq. 4, and thereby the scaling coefficient y to convert each measurement of wavelength into

metres. The average crest to crest distance was calculated for each wave train by dividing the total wave train length by the number of waves in the train. Boulder dimensions were also obtained using Eq. 4.

Bed topography and topographic change

To define changes in the valley and channel geometries in response to flash flood events, differential GPS surveys (dGPS) of the Belham Valley floor between the coast and point E (Fig. 3C), were undertaken in February 2012 and March 2013, and compared with earlier surveys (Barclay *et al.*, 2007; Sušnik, 2009; Alexander *et al.*, 2010; Darnell, 2010; Darnell *et al.*, 2010). A Leica AT302 GPS antenna (vertical accuracy ±10 to 20 mm, horizontal accuracy 10 to 20 mm; Leica Geosystems Inc., Norcross, GA, USA) was used in kinematic mode on-foot. A quasi-systematic method was adopted, in which the perimeter of individual topographic features, such as bars and banks (top-edge and base), was surveyed, in addition to a series of transects across the valley. Leica Geo-Office Software™ was used to post-process the data with reference to the base station (MVO1), orbit information, precise ephemeris and antenna calibration. Resolved points were assessed for quality, and points with a root-mean-square error >20 mm were removed from the data set. Points for each survey were interpolated in ESRI ArcMap™ software using a series of hard breaklines (along abrupt changes in slope) and a hard clip, which restricted the interpolation to the point cloud. Constrained Delaunay triangulation was used to connect the points in a series of triangles. Triangulated Irregular Network (TIN) surfaces retain information on steep breaks in slope if these are delineated during the data collection (Brasington *et al.*, 2000; Darnell, 2010), providing useful markers of terrace erosion and channel migration between surveys. The TINs were converted directly to an elevation raster (digital elevation model – DEM) with a regular 10 × 10 m grid using a linear interpolation. Vertical accuracy is ±30 to 40 mm. Elevation change and volumetric change related to flash floods were calculated by differencing the DEMs.

Between the dGPS surveys in February 2012 and March 2013, only one large flash flood (lasting over 24 h with multiple peaks in discharge) occurred, on 13 to 14 October 2012. In addition, there were 25 small to moderate events that remained within sub-channels, did not modify bed elevation by more than the DEM error and left little or no trace in the sediment record.

13 to 14 October 2012 flash flood measurements

Images from the permanent monitoring camera were sampled systematically and analysed at 900-second intervals between 16:15:00 Coordinate Universal Time (UTC) 13 October 2012 and 22:00:00 UTC 14 October 2012. Local seismicity was recorded on three seismometers (MBLY, MBGH and MBGB; Fig. 3C). Direct rainfall measurement was by a tipping-bucket rain gauge on a Vantage Pro 2 weather station (station SGH2011 – Davis Instruments Corporation, Hayward, CA, USA; Fig. 3C), in the Belham Catchment at 325 m above sea-level. The rain gauge ceased functioning, just after 4:00:00 UTC on 14 October 2012. Rainfall intensity was estimated from Mètèo-France Guadeloupe rainfall radar images at 15-minute intervals. The radar time series correlates well with the timing of rainfall peaks registered on the SGH2011 weather station on 13 October, but underestimates measured peak rainfall intensity by 46%. This underestimate is based on the comparison of radar-derived estimates with rain gauge data when it was operational. Therefore, radar data intensity estimates on 14 October 2012 were adjusted accordingly.

Combined with seismic data and rainfall measurements, images at the camera site were used to monitor changing stage (estimated from proportion of the valley floor occupied by flow), timing of peak flow stages, the occurrence, geometry and size of stationary water-surface waves, the size of moving boulders, apparent flow turbulence and the timing of rainfall. Valley width occupied by flow served as a proxy for discharge, given the shallow sub-channel depth and high width:depth ratio of 112.

Hand-held cameras (still and video) provided supplementary images of conditions downstream (sites B1 and B2; Fig. 3C). This section of valley was highly modified by aggregate mining, but remained accessible during flood events. Flow velocity was estimated using a float distance transit at sites B1 and B2 (Fig. 3C), during daylight. This method provides an estimate of surface flow velocity along the travel vector of the floating object. These were the only direct measurements of velocity acquired during the flood event. Flow velocity and depth at the camera site were estimated using water-surface wave geometry, and Eqs 1 and 2. Suspended

sediment was sampled using a 'bucket' method with a 500 ml container at mid-water depth at the edge of the main channel at site B2 (Fig. 3C), during waxing flow (16:16:00 UTC 13/10/12, 16:21:00 UTC, 13/10/12) and during waning flow (21:00:00 UTC, 14/10/12). The dried mass was used to estimate the suspended sediment concentration and the grain-size distribution from laser-diffraction with a Malvern Mastersizer 2000 (Malvern Instruments Limited, Malvern, UK; Table 2).

Palaeoflow velocity estimates from grain size

Two methods were used to estimate flow velocity using the dimensions of large clasts observed to move in the flash flood and in the event deposit (Table 3). The Clarke (1996) method estimates the minimum critical force needed to initiate the movement of a submerged boulder in a steady flow. The critical flow velocity is calculated from the drag force (C_D) acting on the boulder, fluid density (ρ) and the cross-sectional area of the boulder. Both cubic and spherical shapes are considered and results averaged to estimate critical stream velocity. The Alexander & Cooker (2016) method considers forces acting on a boulder in unsteady flow, including an impulsive force generated by change in flow conditions.

13 to 14 October 2012 flash flood study sites

Two key sites within a study reach are discussed in this article: the camera site and the trench site (Fig. 3C). A sample transect across the camera site was surveyed before the flash flood on 12 October 2012 (Fig. 7A) and after the flood on 15 October 2012 (Fig. 7C). Grain size was estimated at 0·1 m intervals along this transect, and the presence or absence of vegetation recorded. Silt and sand grade (<2 mm) were classed as a single category, and medium, coarse and very coarse pebbles, cobbles and boulders were measured at each sample point. Geomorphological sketch maps drawn pre-flood and post-flood were used to record changes in channel structure at the camera site. Pre-event surveys showed that the dry valley floor had a gradient of 2·8° and was braided (Fig. 7B and E). The number of sub-channels, their depth and boundary characteristics changed during the flood. Both before and after the flood, the sub-channel depths were <0·2 m and channel floors were sandier than the gravel bar surfaces.

Table 2. Flow conditions at monitoring sites B1 and B2. Reynolds number is calculated as a range to incorporate the error (±0·3 m) for water depth.

Site	Date/time	Floating object	Surface velocity (m sec^{-1})	Estimated mid-depth velocity (m sec^{-1})	Water depth h_m (m) ±0·3 m	Channel width (m)	Suspended sediment concentration (g m^{-3})	Suspended sediment: percentage silt	Suspended sediment: percentage sand	Estimated Reynolds number
B2	14/10/2012 17:58	Wooden log (0·3 m long)	2·55	2·17	0·5	25·5	4869	10·24	89·76	379658–1518631
B1	13/10/12 16:00–17:00	Coconut	0·83	0·71	0·5	29·6	13 290	57·38	42·62	123725–494901

Table 3. Estimates of flow velocity using water-surface wavelengths (using Eq. 1), clasts within the flow (using the methods of Clarke, 1996 and Alexander & Cooker, 2016), deposit lenses (assuming preservation of 38% and 56%) and deposit clasts (using the methods of Clarke, 1996 and Alexander & Cooker, 2016). Equations for the Clarke (1996) method are reviewed in Stokes *et al.* (2012).

Flow				
Estimates from	Water-surface waves		Clast dimensions	
Date	Mean (m sec^{-1})	max (m sec^{-1})	Clarke (1996) method* (m sec^{-1})	Alexander & Cooker (2016) method† (m sec^{-1})
13/10/2012	2·18	3·61	3·37	3·85
14/10/2012	1·82	2·65	2·36	2·69

Deposit						
Estimates from	Lenses				Clast dimensions	
	Preservation 38%		Preservation 56%		Clarke (1996) method* (m sec^{-1})	Alexander & Cooker (2016) method† (m sec^{-1})
	Mean (m sec^{-1})	Max (m sec^{-1})	Mean (m sec^{-1})	Max (m sec^{-1})		
	1·60	3·46	1·32	2·85	2·56	2·37

*Assuming: acceleration of gravity (g) = 9·81 m sec^{-2}, density of clast (ρ_s) = 2650 kg m^{-3}, density of fluid (ρ) = 999·1 kg m^{-3}, bed slope angle (β) = 0·049 radians (camera site), 0·045 radians (trench site), lift coefficient (C_L) = 0·178 (cubic boulder), 0·2 (round boulder), drag coefficient (C_D) = 1·18 (cubic boulder), 0·2 (round boulder). †Assuming the boulder is spherical with a diameter equal to the mean axial length and the friction coefficient (C_F) = 1. The acceleration of flow (a) = 0·5 m sec^{-2}.

Between the October 2012 flash flood and the subsequent field campaign in March 2013, deposits in the accessible (lower) reaches of the valley were incised a small amount (channel depths <0·3 m) by small run-off events (Fig. 3C). Commercial aggregate excavation by backhoe, 400 m downstream of the camera site (Fig. 3C), created a large trench (herein called the trench site) on the north side of the valley creating temporary vertical exposures typically <1·5 m high, extending laterally up to 150 m north-west (Fig. 8E). These provided the best vertical exposure of the 2012 flash flood event deposit, and the only exposure at a site that was previously unmodified by aggregate excavation. The trench was photographed (for example, Fig. 12A), sketched, logged and sampled.

Aerial imagery and a post-event survey transect at the trench site (prior to excavation) showed that the trench crossed a 23 m wide channel with 2·6° bed slope and gravelly surface on the north side of the valley (Fig. 8F). The channel boundaries were relatively unchanged by the 13 to 14 October 2012 flash flood. In November 2010, the bed surface at the trench site was near planar and covered by a thin laterally continuous massive mud layer (Fig. 8A). Small to moderate flash floods between November 2010 and March 2012 modified the bed forming shallow braided channels, and the surface sediment was sand within the channels and sandy-gravel on the bars (Fig. 8C).

THE 13 TO 14 OCTOBER 2012 SEDIMENT-LADEN FLASH FLOOD

The 13 to 14 October flash flood occurred during the passage of Tropical Storm Rafael which deposited 170 mm of rain in 28 h, with a maximum recorded intensity of 61·5 mm h^{-1} and multiple peaks in rainfall (Fig. 9A). The first rain bands from Tropical Storm Rafael caused localized surface run-off and ponding water in trenches on the valley floor, observed at site B2 on 12 October 2012. Rainfall was initially sporadic (Fig. 9A), becoming near continuous from 14:34:00 UTC and flow was sustained by 16:10:00 UTC in a single 1 to 2 m wide channel on the north side of the valley at site B1. Local

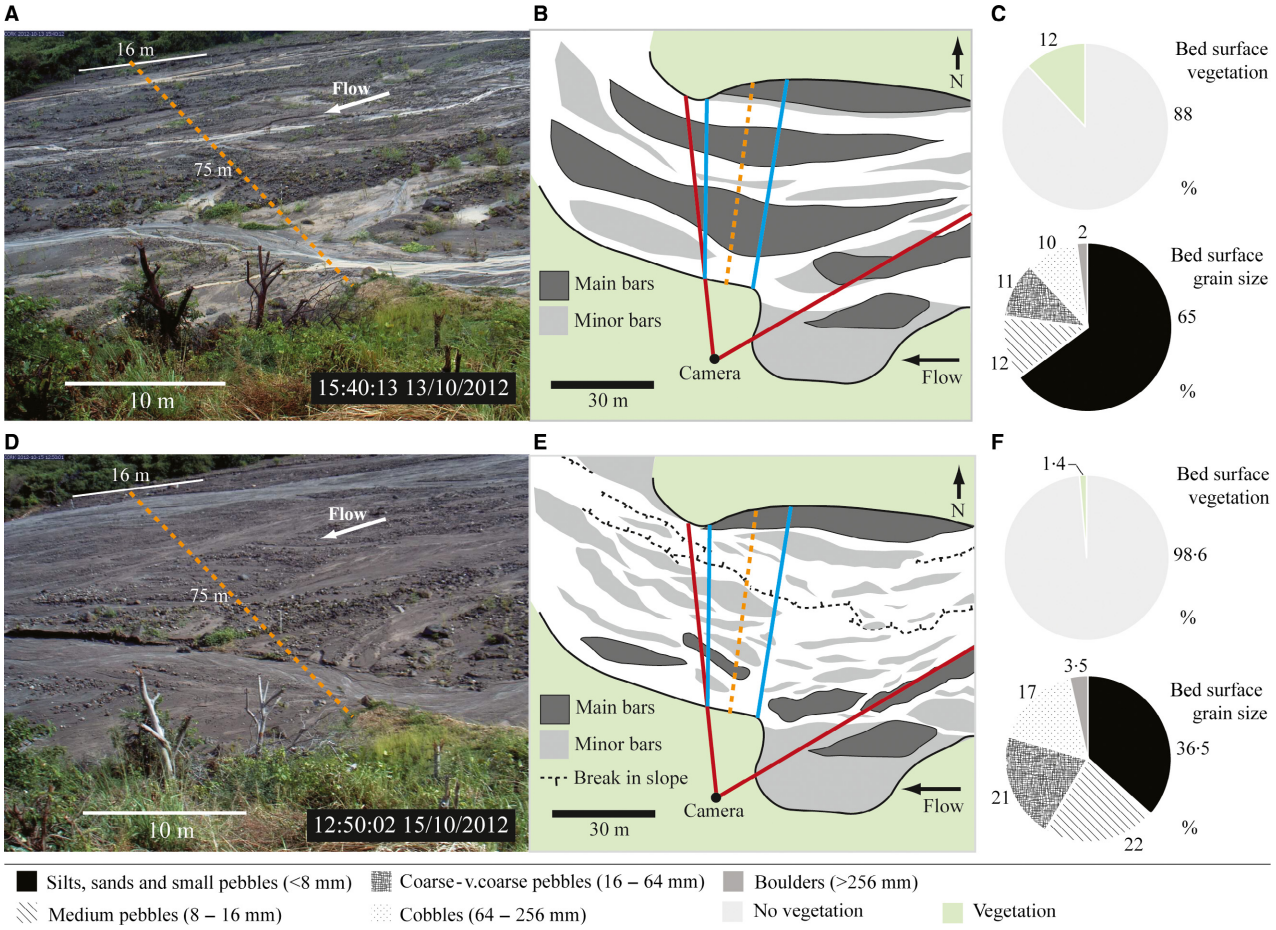

Fig. 7. Camera site on 12 October 2012, before the flash flood. (A) Oblique photograph of the valley floor captured by the remote camera. Orange-dotted line indicates the sample transect and is also shown in the sketch map (B). The red lines delimit the area of the valley floor monitored by the camera. The blue lines delimit the sub-section of the image in which flow features were measured. (C) Bed surface grain size and vegetation cover (key at bottom). (D) Camera site on 15 October 2012, after the flash flood. (E) Sketch map. (F) Bed surface grain size and vegetation cover. Major bars define sub-channel boundaries on the valley floor, whereas minor bars are submerged when flow occupies sub-channels. Sub-channel width varied during the flood: north (<20·0 m), north-middle (<16·5 m), south-middle (<8·5 m) and south (<7·0 m). Some sub-channels coalesced during peak flow (Fig. 9B), but the channel on the south side of the valley remained isolated throughout the flood at this location.

seismicity records confirm flood onset and indicate seven flood peaks (Fig. 9B); these correlate with visual estimates of flow stage, bedload size and quantity from the camera imagery.

The flash flood was highly unsteady, turbulent and sediment-laden. Flow velocity and depth at site B1 at the start of the event were 0·71 m sec^{-1} and 0·5 m. Assuming a water temperature of 15°C, sediment grain density of quartz (2650 kg m^{-3}), with the flow conditions (Table 2), gives Reynolds numbers ($Re = \rho_f Uh/\mu_m$, where ρ_f is the bulk density of the flow and μ_m is the dynamic viscosity) 124 000 to 495 000 on the rising limb of the first flow peak at Site B1 and 380 000 to 1 520 000 on the falling limb of the last flow peak at Site B2. This result is consistent with previous inferences (Barclay *et al.*, 2007; Alexander *et al.*, 2010) that flash floods in this valley are Newtonian and fully turbulent.

Waves and surges in the 13 to 14 October 2012 flash flood – observations

Trains of stationary and upstream migrating waves were prevalent. At the camera site, each train consisted of 3 to 11 waves with wavelengths of 0·32 to 8·33 m (Fig. 9D). Assuming

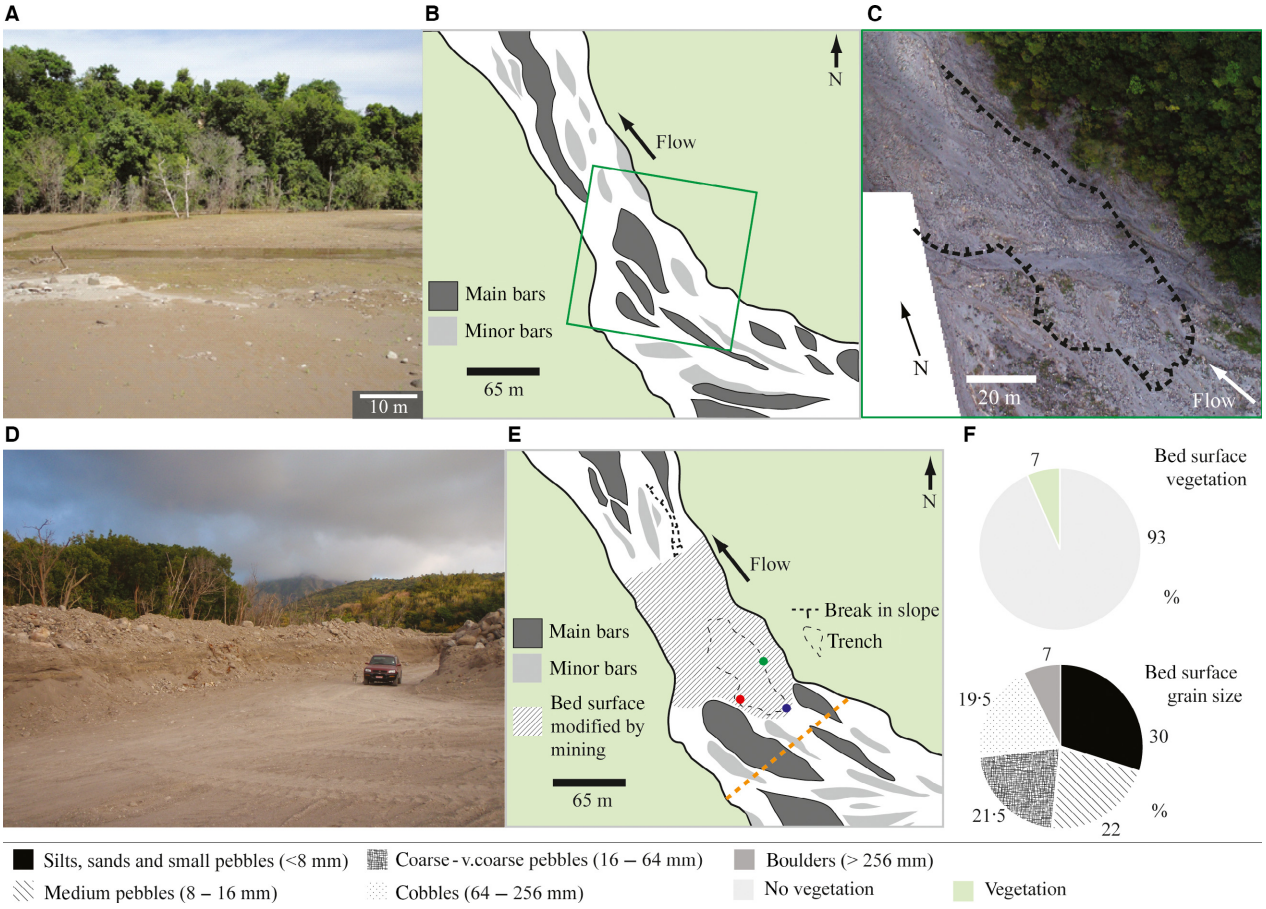

Fig. 8. (A) Trench site before the flash flood. Oblique photograph showing the fines-rich bed surface at the trench site in November 2010; looking upstream to the north side of the valley. Water pooled here following a large flash flood in 2010, resulting in a continuous mud layer within the sediment record. (B) Sketch map, February 2012. Aerial photograph (C) shows the location of the trench (excavated in March 2013), overlain on the February 2012 bed surface. The extent of the aerial photograph is shown by the green rectangle on the geomorphological map (B). (D) Trench site after the flash flood, March 2013. Photograph showing the trench, excavated in March 2013; looking upstream. The trench had a mean depth of 1·5 m, but was *ca* 3 m deep at the upstream-most point. The car for scale is 1·8 m wide. (E) Sketch map, March 2013. A section of the valley bed surface (diagonal lines) was modified by commercial aggregate extraction from early 2013. The trench location is shown by a dashed-edged polygon. Log locations are shown: log 1 (red dot), log 2 (green dot) and log 3 (blue dot). The orange dashed line corresponds to the location of a second sample transect, surveyed on 15 October 2012. (F) Bed surface grain size and vegetation cover (key at bottom).

two-dimensional waves, in the study reach the maximum mean flow velocity, U, was 3·6 m sec^{-1} (Eq. 1), and maximum flow depth, h_m, was 1·3 m (Eq. 2). Although most waves appear to be two-dimensional, the perspective and image resolution of photographs could mean that there were some three-dimensional waves that were not identified. Assuming a water temperature of 15°C and sediment grain density of quartz (2650 kg m^{-3}), the flow conditions give *Re* values of 1 620 000 to 2 620 000, based on suspended sediment concentrations measured at sites B1 and B2 (Table 2). Table 4 contains estimates of maximum mean flow velocity and maximum flow depth for each sub-channel, showing the variation in flow conditions across the valley floor at this location.

At the camera site, waves extended partially or fully across sub-channels, varying with time. The first wave train formed shortly after occupation of the north sub-channel and persisted for *ca* 10 min, reducing in amplitude and disappearing as flow depth increased, but a new wave train formed at the same place in the channel

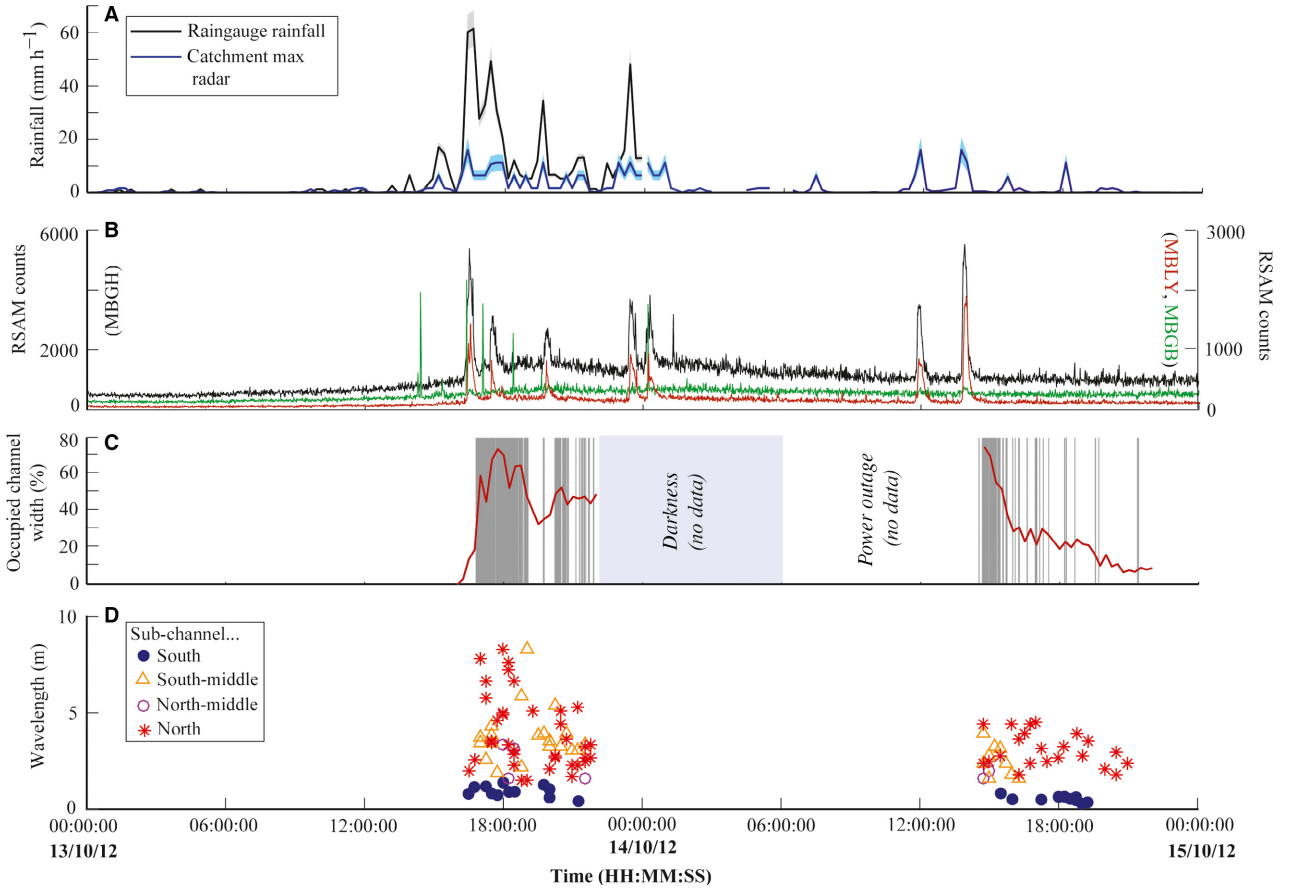

Fig. 9. (A) Rainfall intensity calculated over 900-second intervals from the SGH2011 rain gauge (Fig. 3C) and the maximum pixel value for the Belham Catchment from the Mètèo-France Guadeloupe rainfall radar. (B) One-minute real-time seismic amplitude (RSAM) from MBLY, MBGH and MBGB. (C) Percentage of valley-floor width occupied by flow (red), passage of bores at the camera site (grey bars) and camera functionality. (D) The average wavelengths of water-surface wave trains present in the sample area (Fig. 6A) of camera images between 16:15:00 UTC 13/10/2012 and 22:00:00 UTC 14/10/2012, sampled every 15 min. Each wave train is located within a sub-channel on the valley floor (see Fig. 6B).

Table 4. Estimates of flow velocity (using Eq. 1) and flow depth (using Eq. 2), based on the maximum mean wavelength from wave trains observed at the camera site (Fig. 3C) between 16:15:00 UTC 13/12/2012 and 22:00:00 UTC 14/10/2012 (see Fig. 8D).

		Wavelength, λ (m)			Mean flow velocity, U (m sec^{-1})			Flow depth, h_m (m)		
Date	Sub-channel	Min	Mean	Max	Min	Mean	Max	Min	Mean	Max
13/10/2012	North	0·42	0·94	1·38	0·81	1·19	1·47	0·24	0·63	1·33
13/10/2012	North-middle	1·62	2·44	3·34	1·59	1·92	2·28	0·29	0·61	1·32
13/10/2012	South-middle	1·85	3·81	8·31	1·70	2·40	3·60	0·26	0·39	0·53
13/10/2012	South	1·48	3·96	8·33	1·52	2·42	3·61	0·07	0·15	0·22
14/10/2012	North	1·75	3·10	4·48	1·65	2·18	2·65	0·28	0·49	0·71
14/10/2012	North-middle	1·58	2·54	3·94	1·57	1·97	2·48	0·25	0·40	0·63
14/10/2012	South-middle	1·63	1·81	2·00	1·59	1·68	1·77	0·26	0·29	0·32
14/10/2012	South	0·29	0·54	0·82	0·68	0·91	1·13	0·05	0·09	0·13

within 30 sec. Waves were prevalent in all sub-channels; they grew and remained stationary for up to 9 min, or migrated upstream at rates <1 m sec^{-1}. Migration upstream was not always continuous, and many wave trains paused for short periods (<10 sec) before continuing to migrate; this led to slower rates of migration, *ca* 0·1 m sec^{-1}. Waves which migrated more rapidly tended to break *en masse* (i.e. more than one adjacent wave breaking at the same time), while slower or stationary waves broke individually (Video Clip S1); or sequentially, the breaking of one wave triggering the breaking of adjacent waves (Video Clip S2). Sometimes waves did not break, but dissipated as local flow conditions changed. Waves tended to reduce in height or disappear, when rain fell directly into the flow because flow depth locally (temporarily) increased (and Froude number decreased). One wave train in the south sub-channel persisted for over 60 min before disappearing, and a new wave train formed in its place shortly afterwards (<2 min). Some wave trains grew in length, with the addition of new waves at either end of the wave train. Entire wave trains were observed to change position across the valley floor in response to changes in channel boundaries, as well as migrating upstream.

Wave trains occupied most sub-channels at sites B1 and B2 when visited at 16:16:00, 16:56:00, 17:50:00 and 23:00:00 UTC on 13 October 2012, and at 12:00:00, 13:00:00 and 21:00:00 UTC on 14 October 2012. Visual observations of wave trains at sites B1 and B2 were in-person and with higher resolution image capture, but for significantly shorter duration than at the camera site. At site B1 when waves within trains grew and diminished in height, they also changed between undular and breaking form. Most waves observed were two-dimensional, with wavelengths between 0·3 m and 1·2 m; they persisted for <10 min at locations both in the centre of the channel and near the channel edge. The largest wave train observed (nine waves), with a mean wavelength of 5·4 m (centre of channel at site B1 17:15 to 18:15 on 14 October 2012), contained three-dimensional waves (with a mean transverse wavelength of 3·9 m) which changed between undular and breaking form (Video Clips S3 and S4), mostly remaining stationary with short periods of upstream migration. Some individual waves in the train broke and reformed, but the train as a whole persisted for longer than the one-hour observation period. Flow velocity was estimated as 1·6 m sec^{-1} using Eq. 3; this is lower than flow velocity estimated by float distance transit (Table 2), but is thought to better estimate mean conditions compared with the float measurement, because the water-surface waves persisted for a long period (more than an hour) and covered a larger part of the channel (190 m^2), and hence local variations in velocity with depth or position within the wave train were captured.

Three hundred and forty-nine turbulent surges (bores) were recorded during the daylight hours of the flood, occurring at 6 to 6002 second intervals (Fig. 9C); on average, 108 bores were recorded per hour during the event (minimum, 2 per hour and maximum, 190 per hour). These were downstream propagating and channel wide with distinct breaking fronts (Video Clip S5). The bores travelled at an average velocity of *ca* 6 m sec^{-1} and induced temporary increases in flow depth of up to half a metre; during waxing, flow bores gradually increased the flow stage; however, during waning conditions, depth change was associated with the front and did not increase flow stage. When a bore approached a wave train (within *ca* 10 m), the waves tended to break concurrently generating a localized short-duration upstream surge. Most waves broke during the passage of a bore, and those which did not reduced in height. The bores were not observed at downstream Sites B1 and B2.

At the camera site, moving cobbles and boulders were observed episodically when they were temporarily exposed by flow, or when they were partially submerged. The biggest clast moving had a maximum observed diameter of 0·89 m, at 17:00 13/10/2012 in the north channel. The biggest clast observed in the middle channels and south channel was 0·62 m at 20:30 on 13/10/2012 and 0·4 m at 19:00 on 13/12/2012, respectively.

DEPOSIT SEDIMENTOLOGY

Three vertical sections from the trench are presented herein, located: (i) parallel to flow within the channel; (ii) near-parallel to flow and parallel to the channel edge; and (iii) perpendicular to flow, cross-cutting the centre of the channel (Fig. 8E). Facies boundaries, sedimentary structures and lamination were delineated (Fig. 10), and architectural element diagrams were drawn (Figs 12 to 14). Grain-size analyses of samples are presented in Fig. 11.

The deposits exposed in the trenches consist of: (i) matrix-supported gravel lenses (Gmw); (ii) clast-supported gravel (Gcl), sometimes

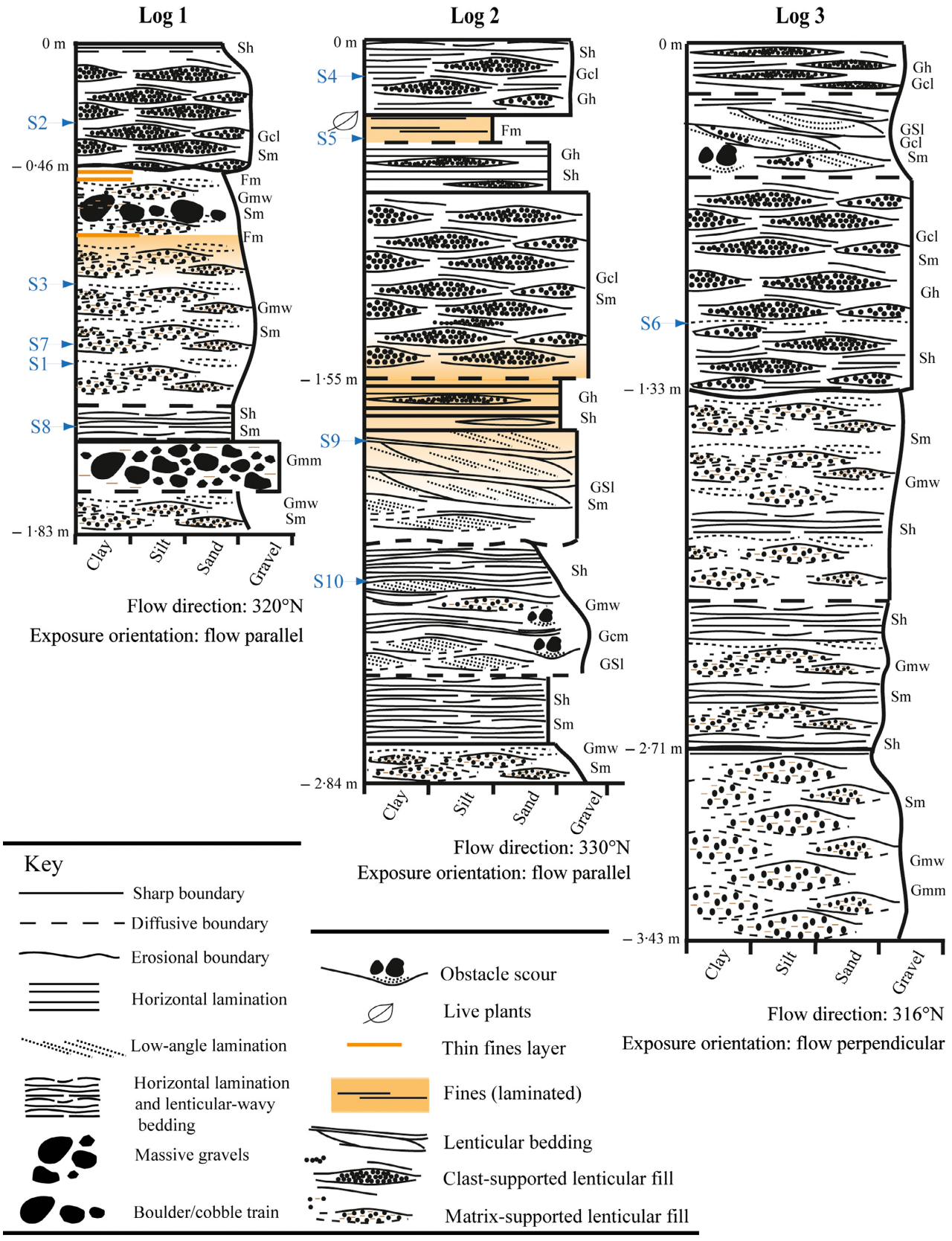

Fig. 10. Sedimentary logs of two flow-parallel and one flow-perpendicular trench sections (Fig. 8E). Table 5 contains the facies code. Sediment sample locations are shown by blue arrows with numeric ID.

organized in a lenticular pattern; (iii) laminated sand (Sh); (iv) massive sand (Sm); (v) silt and fine sand (Fm); (vi) pebbly sand with low-angle cross-beds (GSl); (vii) laminated gravel (Gh); and (viii) beds of massive gravel (Gmm) (Fig. 10; Table 5).

Sedimentary structures formed in the 13 to 14 October 2012 flood event

A distinct sedimentary contact was recognized over >1000 m laterally around the trench faces, at depths varying from 0·45 to 1·4 m below the natural deposit surface (see Logs 1 and 3: Fig. 10). This is interpreted as the base of the 2012 flash-flood deposits. Repeat dGPS surveys in March 2012 and March 2013 record *ca* 0·3 m of aggradation at the trench site, indicating that although there was net aggradation, the pre-event bed was remobilized during the flood (i.e. some bed erosion during the flood followed deposition, scour and fill).

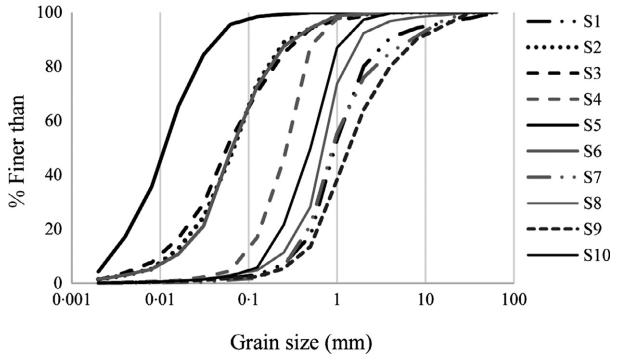

Fig. 11. Grain size of deposit at sampled units (see Fig. 10). The 64·0 to 0·5 mm fraction was determined using dry sieving. Laser-diffraction analysis (using the Malvern Mastersizer 2000) was used to ascertain the grain-size distribution of particles between 0·1 μm and 2·0 mm. The sample number locations are indicated on the logs in Fig. 10.

Table 5. Facies code descriptions.

Lithofacies code	Description
Fm	Massive mud
Sh	Horizontally laminated sand
Sm	Massive sand
GSl	Dipping, laminated pebbly sand
Gh	Laminated gravel
Gmm	Massive matrix-supported gravel
Gmw	Matrix-supported gravel with grading and containing weak wavy lamination
Gcl	Clast-supported gravel from open framework (no matrix) to clast-supported with matrix, graded and laminated

The 13 to 14 October 2012 event deposit includes horizontally laminated sand (Sh), dipping sand and pebble beds (GSl), clast-supported gravel (Gcl) and massive sands (Sm) (Table 5). The event deposit recorded in Log 1 (Fig. 10) predominately consists of clast-supported, open framework to partly open-framework gravel with lenticular structures, interbedded with massive sand (Fig. 12). Lens bases cut into older lenses or massive sand beds. The lowermost lenses cut into pre-event thick massive sand beds (sample S3, grain size shown in Fig. 11). There is a thin layer (<0·02 m) of medium to very coarse sand at the base of most of the gravel lenses (S2, grain size shown in Fig. 11). Where the tops of the lenses are not truncated by other lenses, they are overlain by massive sand. Sand also forms the matrix in the gravel at the top of the lenses. In larger lenses (>0·84 m), the long axis of gravel clasts is inclined towards the lens centre, forming a concave-up pattern. The smallest lenses contain massive finer gravel (relative to the whole deposit). At the site of Log 1, there was one large clast in the event deposit (maximum diameter of 0·37 m), and all others had a maximum diameter <0·13 m.

In the trench face recorded in Log 2 (Fig. 10), the 2012 flash flood deposit is the upper 0·36 m, but in this flow-parallel section, it was partly obscured by collapse of the trench face. A flow-perpendicular section excavated at this location (Fig. 13) exposed inter-bedded planar laminated pebbly sand (Sh, beds <0·02 m thick, Fig. 10) and clast-supported pebble–cobble gravel lenses with erosional bases. Gravel clast fabric forms concave-up structures within most lenses, although some contained convex-upward clast patterns (Fig. 13). The lens basal boundaries are erosional, but the sand matrix within some lenses appears to grade into the surrounding Sh beds. There are also discontinuous beds of clast-supported gravel of large pebble–cobble grade (Gh). The 0·2 m thick massive mud bed (S5 grain size shown in Fig. 11 and structures in Fig. 13), by comparison with dGPS survey data, corresponds to the extensive mud layer deposited on the valley floor at this location in November 2010 (Fig. 8A). It is not possible to distinguish deposits from small–moderate flash floods that occurred between November 2010 and October 2012, but ground observations on

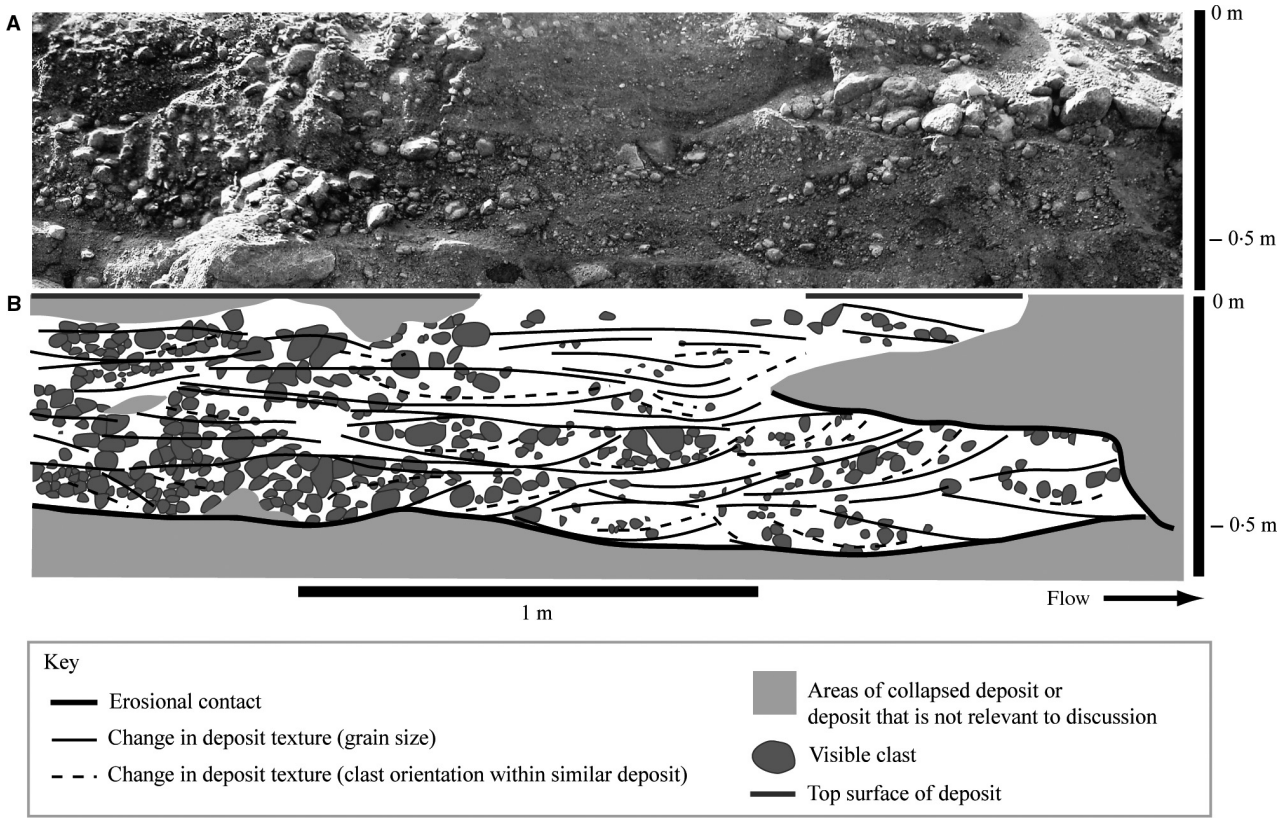

Fig. 12. (A) The 13 to 14 October 2012 flood event deposit in the uppermost 0·46 m of exposure at Log 1 (Figs 8E and 10). Containing clast-supported, matrix-poor, gravel (Gcl) with lenticular structures, interbedded with massive sand (Sm), the main structures are delineated in the line drawing in (B).

15 October 2012 show that this valley-edge location had been occupied by flow. The largest clast in the event deposit at the site of Log 2 was 0·12 m (maximum diameter).

The face recorded in Log 3 (Fig. 10) was perpendicular to flow direction, cross-cutting the sub-channel on the north side of the valley floor (Fig. 8E). In the upper 1·33 m, the 2012 flash flood deposit (Fig. 14) contains clast-supported gravel (Gcl) organized in lenses that truncate and are superimposed on one another. The lens boundaries are delineated by gradational grain-size changes: fine pebbles–boulders within most lenses, to massive and weakly laminated medium to very coarse sand between the lenses (S6, grain size shown in Fig. 11). The horizontal sand beds (for example, at 0·77 m depth) are up to 0·2 m thick, and the planar laminae are discontinuous. The lenses predominantly contain concave-up laminae (finer gravel) and clast fabric patterns (cobble–boulder gravel) that are concordant with lens base, or downlap asymptotically onto the basal surface. Some smaller lenses (<0·2 m) are contained within tabular beds of clast-supported pebble–cobble gravel (Gh). The largest clast in the event deposit at the site of Log 3 had a maximum diameter of 0·18 m.

DISCUSSION

Lens size in relation to antidune wavelength

To infer antidune wavelength from lens size, the lens length (L_L) parallel to flow direction is required (Fig. 1). Lenses are elongate across stream because they are related to waves that extended partly or fully across the channel (rather than three-dimensional antidunes, *cf.* Yokokawa *et al.*, 2010). Lenses were excavated to measure their dimensions in the trench face oriented approximately parallel to the channel axis. In other settings, where flow direction is not easily obtained, it may be possible to use grain fabric to estimate the angle of exposure relative to flow

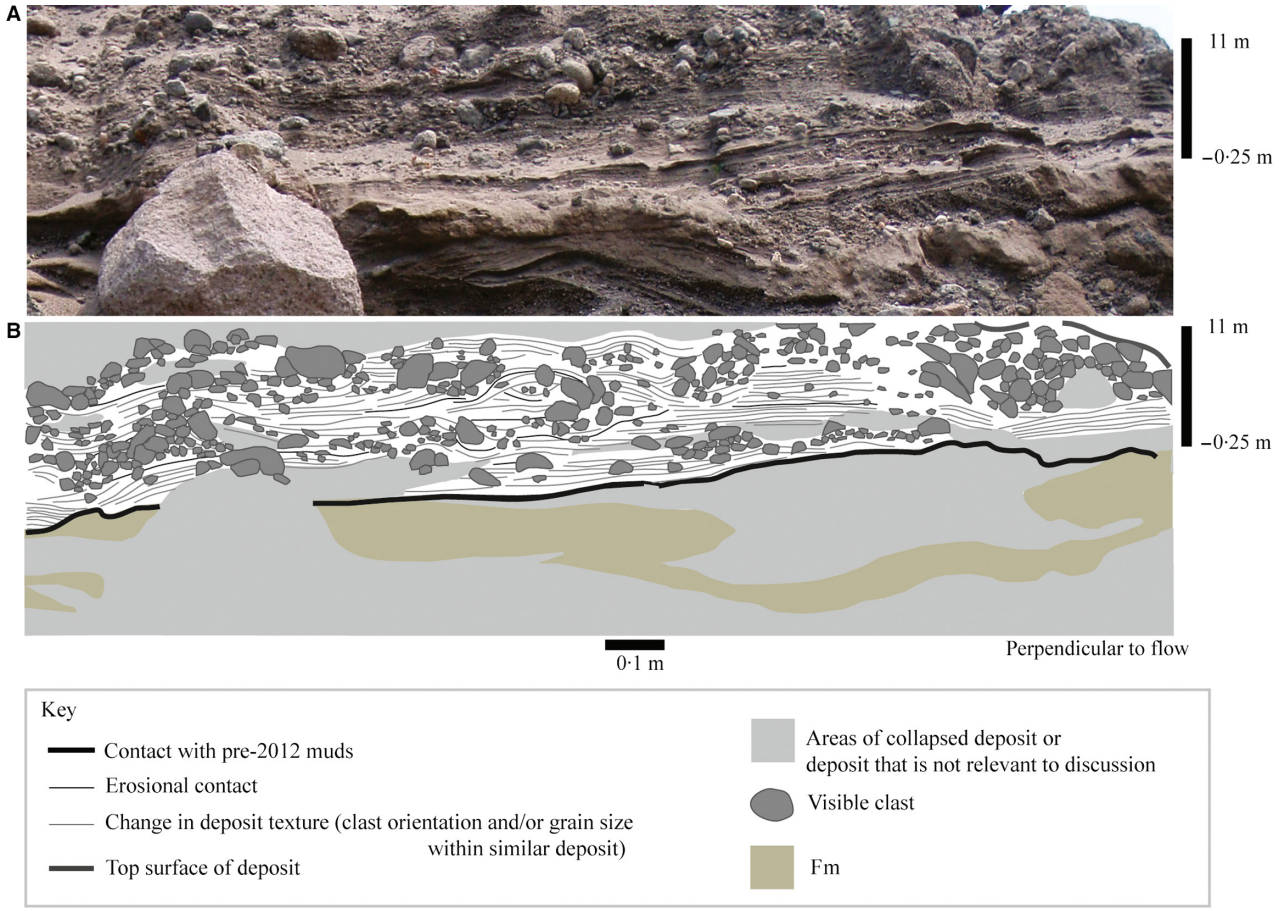

Fig. 13. (A) The 13 to 14 October 2012 flood event deposit in the uppermost 0·36 m of exposure at Log 2 (Figs 8E and 10); the upper 0·11 m of deposit was modified in places at this site during trench excavation. The section contains clast-support gravel lenses (Gcl) and planar laminated sand (Sh) and gravel [Gh, delineated by the line drawing in (B)]. The massive mud (Fm) at the base of the exposed section corresponds to the bed surface at this location in November 2010 (Fig. 8A).

direction to assess flow-parallel lens length. Although this was not assessed directly in this study, strong grain fabrics have been found in experimental and fluvial antidunes (Fig. 15; Yagishita & Taira, 1989; Cheel, 1990; Alexander & Fielding, 1997; Breakspear, 2008) and may be used as a palaeocurrent indicator.

The geometry of an antidune trough is determined by the wavelength of the formative water-surface wave; however, the geometry of the trough preserved as a lens depends not only on water-surface wavelength (antidune wavelength), but on the violence of wave breaking (Blair, 2000), local sediment flux and subsequent bed remobilization. Local sediment flux and the violence of wave breaking vary in both time and space during a flooding event so not all of an antidune is preserved in a sedimentary deposit, and preservation is not uniform. Consequently, individual lens size is unlikely to be an accurate record of an individual stationary wavelength. Mean lens size in one bed, however, may be related to the mean wavelength (temporal and spatial averaging). For example, Alexander *et al.* (2001) observed lenses in flow-parallel sections with an average length of 0·43 m (range 0·19 to 0·75 m, standard deviation 0·13 m) following a flume run with 0·07 m flow depth, 0·76 to 1·14 m wavelength stationary waves and sand addition giving a bed aggradation rate of 0·01 mm sec^{-1}. The ratio of mean lens length L_L to measured water-surface wavelength, λ, in the flume was between 0·38 and 0·56. The range of lens lengths was very comparable to those from a run with no net bed aggradation. In a similar flume experiment with water depth 0·04 m, mean flow velocity 0·85 ms^{-1} and sand-bed aggradation 0·01 mm sec^{-1}, Yokokawa *et al.* (2010) recorded

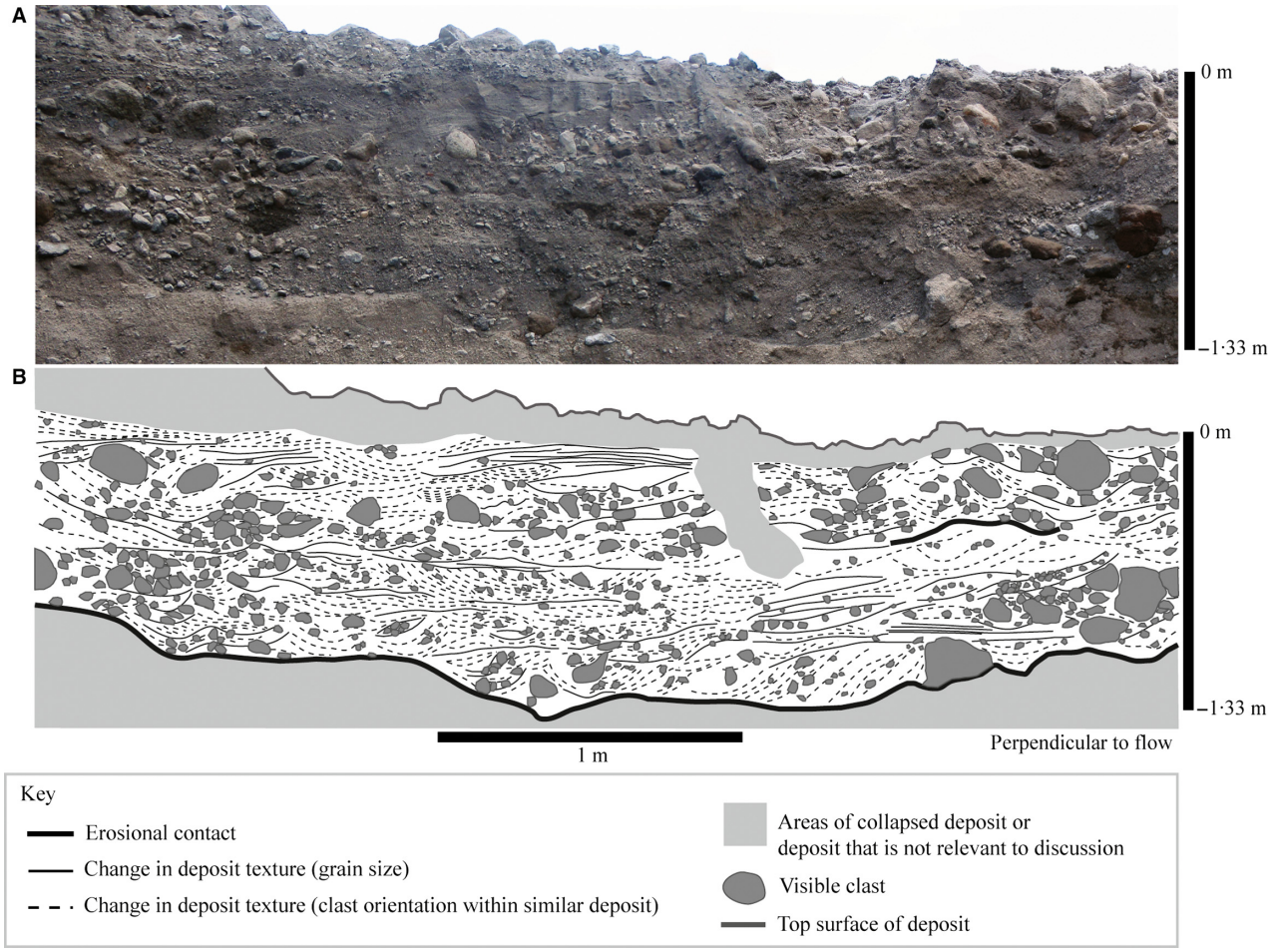

Fig. 14. (A) The 13 to 14 October 2012 event deposit in the uppermost 1·33 m of exposure at Log 3 (Figs 8E and 10). The section contains clast-supported gravel lenses (Gcl) and massive (Sm) to weakly planar laminated sand (Sh) and gravel [Gh, delineated by the line drawing in (B)].

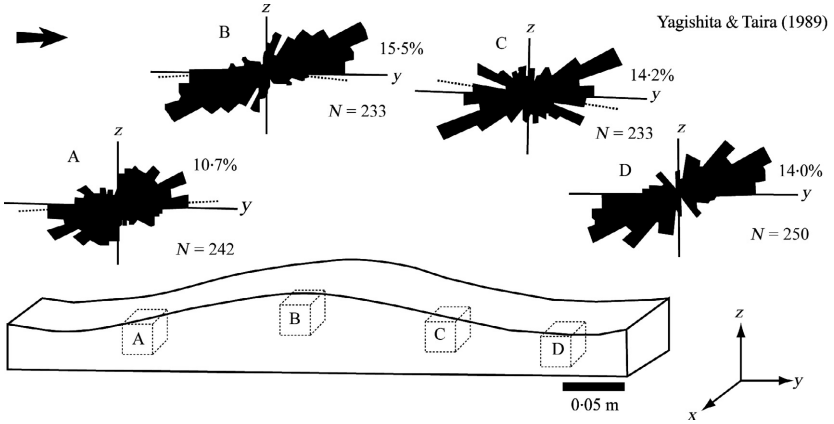

Fig. 15. Imbrication of grains/clasts dipping upstream, on the stoss and lee antidune face formed under non-breaking wave conditions (Yagishita & Taira, 1989). The experimental conditions of each study are provided in Table 1. Yokokawa *et al.* (1999) showed that mean imbrication angle varied cyclically through a vertical antidune section formed by breaking water-surface waves, while Breakspear (2008) showed that clasts were consistently imbricated upstream in non-breaking and breaking wave experiments in gravels.

lenses from 3D antidunes with a mean lens length to water-surface wavelength ratio of 0·4 to 0·5.

Deposits from the 2012 flash flood were only recorded in one flow-parallel section (Log 1: Fig. 10). Gravel lenses had an average length of 0·75 m (range 0·23 to 2·92 m and standard deviation, 0·75 m). Assuming a 38 to 56% preservation (based on preservation in flume experiments), the mean antidune length at the gravel trench site was 1·34 to 1·98 m. This lies within the 1·48 to 8·33 m water-surface wavelengths recorded at the camera site. Using the antidune wavelength range inferred from lenses in the deposit gives estimated flow velocity of 1·43 to 1·76 m sec^{-1} and depths of 0·21 to 0·32 m at the trench site. These estimates are within the range (minimum to maximum) for flow parameters from water-surface waves at the camera site (Table 3).

Lens preservation

The flow conditions estimated from the mean length of lenses associated with the 13 to 14 October 2012 flash flood measured at the trench site are less than the average flow conditions and the maximum peak flow observed at the camera site. There are three possible reasons for this: (i) flow conditions in this part of the channel (400 m from the camera site) were different and water-surface waves that formed had shorter wavelengths compared with those at the camera site, even though the gradient and channel size were comparable; (ii) preservation of lens length was a lesser proportion of the antidune length than preservation observed in flume studies; or (iii) the lenses formed on 14 October, not during peak discharge on 13 October. The camera site and trench site were similar in terms of valley-floor gradient, width, channel pattern and bed surface texture and were situated in close proximity (400 m apart). Average flow conditions at the trench site are thought to have been similar to average conditions at the camera site. This leaves the possibilities that most of preserved lenses formed on the second day of the event and also that the percentage of lens preserved was less than observed in flume experiments.

In the Belham River deposits, there is a strong correlation between lens length and thickness (Fig. 16). As Bridge (1997) and Leclair *et al.* (1997) observed with dune-cross-set preservation, Alexander *et al.* (2001) found that the thickness of antidune lenses related to the depth of scour associated with larger amplitude antidunes and not with bed aggradation rate; indeed, Alexander *et al.* (2001) found it impossible to distinguish between antidune structures from aggrading and non-aggrading beds with the same flow conditions. This is unsurprising when the rate of scour

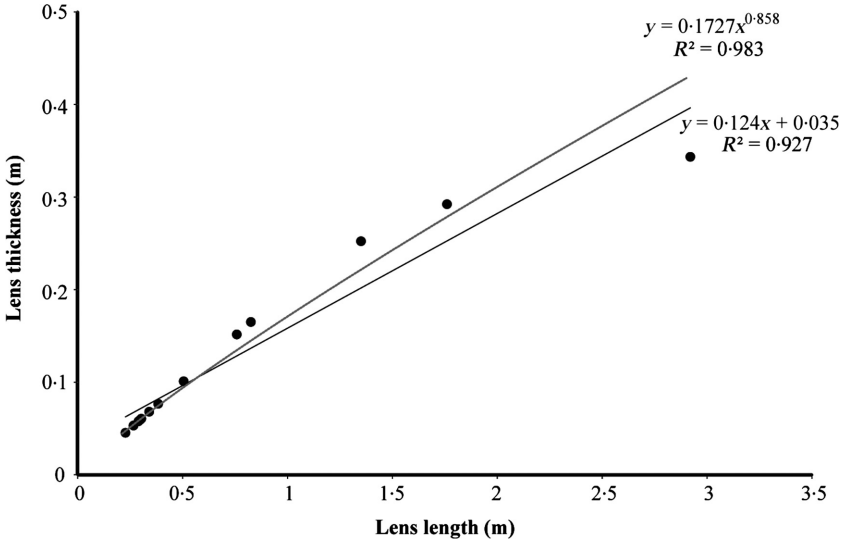

Fig. 16. Lens length versus lens thickness from structures in the 13 to 14 October 2012 flood deposit. The linear trendline and R^2 value indicate a strong correlation between lens length and lens thickness. However, the relationship between lens length and lens thickness is best described by a power law equation. The slight variation around the trend may relate to small variations in the angle between wave axis and channel axis (i.e. not all waves are perpendicular to channel axis), variation in water-surface wave behaviour (breaking, migration) influencing lens base geometry and lens preservation.

and antidune growth following wave breaking in the flume experiments is orders of magnitude faster than mean bed aggradation rate. The same is very likely to be true in most natural settings, where scour and fill will cause near-instantaneous local bed level change rate on the order of 1 to 10 mm sec^{-1}, whereas mean bed aggradation rate, even in the rapidly aggrading Belham system, is 0·003 mm sec^{-1}.

The preserved lens length should increase with parent water-surface wavelength if other conditions are held constant; however, flow was rapidly varying and sediment-laden. Sediment transport during the breaking of hydraulic jumps (bores and water-surface waves) was observed at the camera site during the 13 to 14 October 2012 event. The most visible change was an increase in cobble-boulder transport corresponding with increased discharge, turbulence and bore incidence. In a positive surge moving downstream, if the depth of the bore increases, the ratio of conjugated depths (difference between depth of initial flow and bore depth) increases, and the potential energy loss at the hydraulic jump increases (Cartigny *et al.*, 2014). To satisfy the conservation of mass and momentum, the velocity of the bore must increase with increased bore depth, if initial flow conditions do not change, and this leads to an increase in bore Froude number (Chanson, 2004). As the conjugate depth ratio increases and bore Froude number increases, lens preservation will decrease because higher *Fr* corresponds with increased hydraulic jump size, strength and competence (Khezri & Chanson, 2012b), so that breaking bores and water-surface waves with higher *Fr* are more destructive of the bed surface. Alexander & Cooker (2016) discuss the reason for this greater entrainment of large particles in rapidly changing flow.

Bores observed in this study had Froude numbers ranging from 1·11 to 1·47, corresponding with the undular ($F_r < 1·3$) and breaking, turbulent ($F_r > 1·4$) bores observed by Khezri & Chanson (2012a,b); whereby turbulent breaking bores have been documented to set particles in motion (Khezri & Chanson, 2012b). The bores during the 13 to 14 October 2012 flood appeared most turbulent and more frequently during rising and peak flow stages, and it is thought that these bores exerted more energy to remobilize parts of the bed surface. Given the scale of the bores relative to the water-surface waves, it is likely that they were a major control on lens preservation and the maximum clast size deposited during rising and peak flow stages. These periods are concurrent with the largest water-surface waves measured at the camera site; waves during these periods were quicker to break after formation and broke more violently than waves during waning flow stages.

The largest lens preserved in the deposit (2·92 m) relates to flow velocities between 2·85 m sec^{-1} to 3·46 m sec^{-1} (assuming 38 to 56% preservation). This exceeds the maximum observed flow velocity on 14 October, but just under that estimated for 13 October of 3·61 m sec^{-1} (Table 3). The largest lens was two standard deviations larger than the mean lens length, while the occurrence of water-surface waves on 13 October equating to velocities of 2·85 to 3·46 m sec^{-1} was between one and two standard deviations greater than the mean flow velocity on that day. Flow velocities on 13 October, consistent with the formation of the largest lens size, occurred much more frequently than their preservation would imply. Mean lens length (1·31 to 1·98 m) corresponded with mean wavelength (±1 standard deviation) for times shown in Table 6. The percentile values show that mean lens length is representative of mean conditions measured at the camera site at the onset of flow (16:30:00 to 16:45:00 UTC 13/10/2012) and in waning stages (from 17:15:00 UTC 14/10/2012). The mean lens length underestimates mean wavelength between these times, but is still within range of observed water-surface wavelength. The occurrence of bores was below the average number per hour (108) for all records in Table 6 after 18:30:00 UTC 13/10/2012, and very few bores (<10) were observed after 18:00:00 UTC 14/10/2012, corresponding with declining discharge and mean water-surface wavelength (mean flow velocity).

Estimates of velocity from the largest boulder in the deposit (Table 3) corresponded well with average flow conditions on 13 October and were closer to maximum flow conditions on 14 October. However, the largest clast was nearly three times the size of the next largest in the event deposits (of 0·18 m), equating to flow velocities of 1·78 m sec^{-1} and 1·86 m sec^{-1} (the Alexander & Cooker, 2016; and Clarke, 1996; methods, respectively). The Alexander & Cooker (2016) method is considered more applicable than the Clarke (1996) method in these settings, because the method considers forces in unsteady flow, even though acceleration could not be measured. This figure underestimates the mean flow velocity on 13 October but is close to the mean flow velocity on 14 October. In this case, the Alexander & Cooker (2016) method applied to

Table 6. Water-surface wave measurements at the camera site during 13 to 14 October 2012 flood event, when mean wavelength (±1 standard deviation) corresponded with mean lens length (1·31 to 1·98 m).

Date Time	Number of wave trains measured	Mean wavelength (m)	Standard Deviation	Percentile score (x = 1·31 m)	Percentile score (x = 1·98 m)	Discharge (% of valley floor occupied by flow)	Bore frequency (number per hour)
13/10/2012 16:30	2	1·40	0·85	45·62	75·17	13·77	96
13/10/2012 16:45	2	1·88	1·03	29·12	53·98	18·86	119
13/10/2012 17:15	4	4·04	2·57	14·46	21·19	44·91	160
13/10/2012 17:45	3	2·41	2·01	29·46	41·68	73·65	190
13/10/2012 18:15	5	4·14	3·13	18·14	24·51	52·53	137
13/10/2012 18:30	6	3·16	1·89	16·35	26·76	64·34	115
13/10/2012 18:45	3	3·18	2·39	21·77	30·85	64·71	89
13/10/2012 19:00	2	4·93	4·79	22·36	26·76	47·90	61
13/10/2012 19:44	2	2·60	1·89	24·83	37·07	35·58	47
13/10/2012 20:00	5	2·11	1·30	26·76	46·02	37·71	43
13/10/2012 21:00	3	2·33	0·67	6·30	29·81	47·78	50
13/10/2012 21:15	4	2·77	2·03	23·89	34·83	46·82	50
13/10/2012 21:30	5	2·68	0·70	2·56	15·87	47·90	33
14/10/2012 14:45	5	2·94	1·19	8·53	20·9	74·79	69
14/10/2012 15:00	4	2·23	0·55	4·65	32·64	70·03	70
14/10/2012 15:30	3	2·24	1·25	22·66	41·68	51·93	73
14/10/2012 16:00	3	2·27	2·01	31·92	44·43	28·94	45
14/10/2012 16:15	3	2·36	1·14	17·88	37·07	31·06	35
14/10/2012 16:45	2	3·40	1·50	8·08	17·11	30·05	17
14/10/2012 17:15	2	1·83	1·88	39·36	79·1	30·18	12
14/10/2012 18:00	2	1·66	1·44	40·52	58·71	19·28	7
14/10/2012 18:15	2	1·96	1·85	36·32	50·4	23·20	7
14/10/2012 18:30	1	0·54		100	100	20·18	7
14/10/2012 18:45	3	1·68	1·97	42·47	55·96	24·53	7
14/10/2012 19:00	2	1·51	1·72	45·22	60·64	22·00	6
14/10/2012 19:15	2	1·96	2·27	38·59	50·4	21·30	4
14/10/2012 20:30	2	2·37	0·88	11·31	33	11·13	3

the largest boulder in deposit gives a fair estimate of velocity, but the other boulders in the deposits were much smaller and would have misrepresented the velocity in the flow. The boulders also generate velocity estimates less than the observed peak flow velocities, supporting the idea that most if not all of the event deposit was formed after the peak flow and during waning conditions. The lens size does not rely on the size of sediment available and therefore may be a more universally useful means to estimate flow conditions than maximum clast size.

This study confirms that lens architecture can be related to antidunes not only for sand beds (*cf.* Alexander *et al.*, 2001; Duller *et al.*, 2008) but also for gravel. This demonstrates the potential to use the ratios of water-surface wavelength (and antidune wavelength) to lens size as a record of time-averaged conditions during a flood event. Instantaneous flow metrics can otherwise be difficult to measure, even within a flume environment, in flows in which there is spontaneous wave breaking and rapid feedback between the flow and bed, fast, localized variation in depth, velocity and suspended sediment concentration. The application of Alexander *et al.* (2001) ratios in this study demonstrates that mean lens length may underestimate mean flow conditions in rapidly varying natural channels. More data are required from different natural settings to improve application of the relationship between antidune length and preserved lens length. It is not known how lens preservation varies with patterns of wave breaking, sediment mobility or Froude number, because the architecture of few antidune beds has been documented.

CONCLUSIONS

Numerous trains of water-surface wave were observed in the October 2012 flash flood in the Belham Valley on Montserrat and these played an important role in sedimentary processes. Water-surface wave trains are prevalent in other similar floods in the Belham Valley and in a multitude of other environments.

The October 2012 event deposits are dominated by lenses that are interpreted as structures formed by antidunes developing and changing during the growth, breaking and dissipation of stationary water-surface wave trains. The characteristics of the gravel lenses are similar to the sand lenses formed by antidunes in flume experiments (*cf.* Alexander *et al.*, 2001). This confirms that even where the antidune bedforms are not preserved, diagnostic structures may be recognized and lens architecture can be related to antidunes in both sand and gravel deposits.

Mean lens size in a bed is a function of both antidune wavelength (and thus the water-surface wavelength) and the degree of antidune preservation. Thus, lens length, measured parallel to the flow direction, as indicated, for example, by grain fabric, can be used to estimate palaeoflow velocity and depth, through the relationship between antidune wavelength to water-surface wavelength. Using the preservation fractions of 0·38 to 0·56 calculated by Alexander *et al.* (2001) for sand lenses in a flume experiment applied to the gravel lenses observed in Belham Valley event deposit underestimates average flow conditions over an entire event and is nearer to that on the afternoon of 14 October 2012. Flow velocity estimated from maximum clast size in the same deposit gives velocities close to the mean on 13 October and the maximum on 14 October, confirming that the deposit mostly or entirely formed after the peak flow. It is likely that most if not all of the lenses formed during waning flow (with peak flow lenses having been reworked), although it is also possible that the preservation of gravel lenses was less than sand lens preservation in the Alexander *et al.* (2001) flume experiments. This demonstrates that antidune lenses are a good indicator of flow conditions (although they may underestimate peak flow) and, because they do not rely on grain-size availability, they may be more universally applicable than competence methods in some settings.

ACKNOWLEDGEMENTS

The work was funded by NERC grant NE/I528285/1, and significant support was provided by the Montserrat Volcano Observatory. The authors thank Professor Jim Best, Dr Matthieu Cartigny, Dr Rob Duller, Professor Miwa Yokokawa and Dr Vern Manville for their constructive comments on an earlier version of the manuscript.

NOMENCLATURE

a	Acceleration of flow (*cf.* Alexander & Cooker, 2016)
β	Bed slope angle (radians, *cf.* Clarke, 1996; Stokes *et al.*, 2012)

C	Solids fraction (volume of solids/bulk volume of fluid)
C_L	Coefficient of lift (*cf.* Clarke, 1996; Stokes *et al.*, 2012)
C_D	Coefficient of drag (*cf.* Clarke, 1996; Stokes *et al.*, 2012)
C_F	Coefficient of friction (*cf.* Alexander & Cooker, 2016)
SC	Sediment mass concentration (g m^{-3})
Fr	Froude number
g	Acceleration due to gravity
h	Flow depth
h_m	Mean flow depth
T	An interval of time
U	Mean streamwise fluid velocity
$u(t)$	Magnitude of fluid velocity variation in time in the downslope direction = $u_0 + u_1(t)$
u_0	Time-averaged fluid velocity
ρ	Density of water at 15°C (999·1 kg m^{-3})
ρ_f	Bulk density of the fluid
ρ_s	Density of sediment (quartz 2650 kg m^{-3})
λ	Streamwise wavelength of water-surface waves
λ_a	Antidune wavelength
λ_t	Transverse wavelength of 3D waveform
L_L	Lens length
μ	Viscosity (water at 15°C = 0·001139 kg m^{-1} sec^{-1})
μ_m	Effective viscosity of sediment–water mix

REFERENCES

Alexander, J. and **Cooker, M.J.** (2016) Moving boulders in flash floods and estimating flow conditions using boulders in ancient deposits. *Sedimentology*, **63**, 1582–1595.

Alexander, J. and **Fielding, C.R.** (1997) Gravel antidunes in the tropical Burdekin Rivers, Queensland, Australia. *Sedimentology*, **44**, 327–337.

Alexander, J., **Bridge, J.S.**, **Cheel, R.J.** and **LeClair, S.F.** (2001) Bedforms and associated sedimentary structures formed under supercritical water flows over aggrading sand beds. *Sedimentology*, **48**, 133–152.

Alexander, J., **Barclay, J.**, **Sušnik, J.**, **Loughlin, S.C.**, **Herd, R.A.**, **Darnell, A.** and **Crosweller, S.** (2010) Sediment-charged flash floods on Montserrat: the influence of synchronous tephra fall and varying extent of vegetation damage. *J. Volcanol. Geoth. Res.*, **194**, 127–138.

Allen, J.R.L. (1982) *Sedimentary Structures*, Vol **1–2**, Elsevier, Amsterdam, Netherlands, 592 pp.

Andrews, E.D. (1983) Entrainment of gravel from naturally sorted riverbed material. *Geol. Soc. Am. Bull.*, **94**, 1225–1231.

Barclay, J., **Alexander, J.** and **Sušnik, J.** (2007) Rainfall-induced lahars in the Belham valley, Montserrat, West Indies. *J. Geol. Soc. London*, **164**, 815–827.

Barwis, J.H. and **Hayes, M.O.** (1985) Antidunes on modern and ancient washover fans. *J. Sed. Petrol.*, **55**, 907–916.

Billi, P. (2011) Flash flood sediment transport in a steep sand-bed ephemeral stream. *Int. J. Sed. Res.*, **26**, 193–209.

Blair, T.C. (2000) Sedimentology and progressive tectonic unconformities of the sheetflood-dominated Hell's Gate alluvial fan. *Death Valley Calif. Sed. Geol.*, **132**, 233–262.

Blair, T.C. and **McPherson, J.G.** (1999) Grain-size and textural classification of coarse sedimentary particles. *J. Sed. Res.*, **69**, 6–19 A.

Brasington, J., **Rumsby, B.T.** and **Mcvey, R.A.** (2000) Monitoring and modelling morphological change in a braided gravel-bed river using high resolution GPS-based survey. *Earth Surf. Proc. Land.*, **25**, 973–990.

Breakspear, R. (2008) *Hydrodyanmics and sedimentary structures of antidunes in gravel and sand mixtures*, Unpublished PhD thesis, University of Southampton, 355 pp.

Bridge, J.S. (1997) Thickness of sets of cross strata and planar strata as a function of formative bed-wave geometry and migration, and aggradation rate. *Geology*, **25**, 971–974.

Browne, G.H. and **Plint, G.** (1994) Alternating braidplain and lacustrine deposition in a strike-slip setting: the Pennsylvanian Boss Point Formation of the Cumberland Basin, maritime Canada. *J. Sed. Res.*, **64**(1b), 40–59.

Burke, M.J., **Woodward, J.**, **Russell, A.J.**, **Jay Fleisher, P.** and **Bailey, P.K.** (2010) The sedimentary architecture of outburst flood eskers: a comparison of ground-penetrating radar data from Bering Glacier, Alaska and Skeiðarárjökull, Iceland. *Geol. Soc. Am. Bull.*, **122**, 1637–1645.

Carling, P.A., **Hoffmann, M.**, **Blatter, A.S.** and **Dittrich, A.** (2002a) Drag of emergent and submerged rectangular obstacles in turbulent flow above bedrock surface. In: *Rock Scour Due to Falling High-Velocity Jets* (Eds A.J. Schleiss and E. Bollaert), pp. 83–94. Swets & Zeitlinger, Lisse.

Carling, P.A., **Hoffmann, M.** and **Blatter, A.S.** (2002b) Initial motion of boulders in bedrock channels. *Ancient floods, modern hazards: principles and application of paleoflood hydrology. Water Sci. Applicat.*, **5**, 147–160.

Carling, P.A., **Burr, D.M.**, **Johnsen, T.F.** and **Brennand, T.A.** (2009) A review of open-channel megaflood depositional landforms on Earth and Mars. In: *Megaflooding on Earth and Mars* (Eds D.M. Burr, P.A. Carling and V.R. Baker), pp. 33–49. Cambridge University Press, UK, Cambridge.

Carling, P., **Jansen, J.** and **Meshkova, L.** (2014) Multichannel rivers: their definition and classification. *Earth Surf. Proc. Land.*, **39**, 26–37.

Cartigny, M.J.B., **Ventra, D.**, **Postma, G.** and **van Den Berg, J.H.** (2014) Morphodynamics and sedimentary structures of bedforms under supercritical-flow conditions: new insights from flume experiments. *Sedimentology*, **61**, 712–748.

Cassidy, M., **Taylor, R.N.**, **Palmer, M.R.**, **Cooper, R.J.**, **Stenlake, C.** and **Trofimovs, J.** (2012) Tracking the magnetic evolution of island arc volcanism: insights from a high-precision Pb isotope record of Montserrat, Lesser Antilles. *Geochem. Geophys. Geosyst.*, **13**, 1–19.

Chanson, H. (2004) *Hydraulics of Open Channel Flow*. Butterworth-Heinemann, Oxford, UK, 650 pp.

Cheel, R.J. (1990) Horizontal lamination and the sequence of bed phases and stratification under upper flow regime conditions. *Sedimentology*, **37**, 517–529.

Church, M. (1978) Paleohydrological reconstructions from a Holocene valley fill. In: *Fluvial Sedimentology* (Ed. A.D. Miall), Canadian Society of Petroleum Geologists, Memoir, **5**, 743–772.

Church, M., **Hassan, M.A.** and **Wolcott, J.F.** (1998) Stabilizing self-organized structures in gravel-bed stream channels: field and experimental observations. *Water Resour. Res.*, **34**, 3169–3179.

Clarke, A.O. (1996) Estimating probable maximum floods in the Upper Santa Ana Basin, Southern California, from stream boulder size. *Environ. Eng. Geosci.*, **2**, 165–182.

Costa, J.E. (1983) Paleohydraulic reconstruction of flash-flood peaks from boulder deposits in the Colorado Front Range. *Geol. Soc. Am. Bull.*, **94**, 986–1004.

Cotter, E. and **Graham, J.R.** (1991) Coastal plain sedimentation in the late Devonian of southern Ireland; hummocky cross-stratification in fluvial deposits? *Sed. Geol.*, **72**, 201–224.

Darnell, A.R. (2010) Application of geographical information systems to lahar hazard assessment on an active volcanic system, Ph.D. Thesis, University of East Anglia, UK.

Darnell, A.R., **Lovett, A.A.**, **Barlcay, J.** and **Herd, R.A.** (2010) An application-driven approach to terrain model construction. *Int. J. Geogr. Inf. Sci.*, **24**, 1171–1191.

Douxchamps, D., **Devriendt, D.**, **Capart, H.**, **Craeye, C.**, **Macq, M.** and **Zech, Y.** (2005) Stereoscopic and velocimetric reconstructions of the free surface topography of antidune flows. *Exp. Fluid.*, **39**, 533–551.

Doyle, E.E., **Cronin, S.J.**, **Cronin, J.S.** and **Thouret, J.C.** (2011) Defining conditions for building and debulking in lahars. *Geol. Soc. Am. Bull.*, **123**, 1234–1246.

Duller, R.A., **Mountney, N.P.**, **Russell, A.J.** and **Cassidy, N.C.** (2008) Architectural analysis of a volcanistic jökulhlaup deposit, Southern Iceland: sedimentary evidence for supercritical flow. *Sedimentology*, **55**, 939–964.

Fielding, C.R. (2006) Upper flow regime sheets, lenses and scour fill: extending the range of architectural elements for fluvial sediment bodies. *Sed. Geol.*, **190**, 227–240.

Foley, M.G. (1977) Gravel-lens formation in antidune-regime flow- a quantitative hydrodynamic indicator. *J. Sed. Petrol.*, **47**, 738–746.

Fralick, P. (1999) Paleohydraulics of chute-and-pool structures in a Paleoproterozoic fluvial sandstone. *Sed. Geol.*, **125**, 129–134.

Froude, M.J. (2015) *Lahar dynamics in the Belham River Valley, Montserrat: application of remote camera-based monitoring for improved sedimentological interpretation of post-event deposits*. PhD Thesis, University of East Anglia, UK pp. 360

Fujiwara, O. and **Tanigawa, K.** (2014) Bedforms record the flow conditions of the 2011 Tohoku-Oki tsunami on the Sendai Plain, northeast Japan. *Mar. Geol.*, **358**, 79–88.

GEBCO (2014) General Bathymetric Chart of the Oceans. Available at: http://www.gebco.net/data_and_products/gridded_bathymetry_data/ (accessed 3/6/2016).

Grant, G.E. (1997) Critical flow constrains flow hydraulics in mobile-bed streams: a new hypothesis. *Water Resour. Res.*, **33**, 349–358.

Gray, W.M. (1979) Hurricanes: their formation, structure and likely role in the tropical circulation. In: *Meteorology Over the Tropical Ocean* (Ed. D.B. Shaw), pp. 155–218. Royal Meteorological Society, Bracknell.

Hand, B.M. (1974) Supercritical flow in density currents. *J. Sed. Petrol.*, **44**, 637–648.

Harms, J. and **Fahnestock, R.** (1965) Stratification, bedforms, and flow phenomena (with an example from the Rio Grande). In: *Primary Sedimentary structures and their hydrodynamic interpretation* (Ed. G.V. Middleton), Society of Economic Palaeontologists and Mineralogists, Special Publication **12**, 84–115.

Hayes, S., **Montgomery, D.** and **Newhall, C.** (2002) Fluvial sediment transport and deposition following the 1991 eruption of Mount Pinatubo. *Geomorphology*, **45**, 211–244.

Jones, J.B. and **Mulholland, P.J.** (1999) *Stream and Ground Waters*. Elsevier, California, CA, 425 pp.

Jopling, A. and **Richardson, E.V.** (1966) Backset bedding developed in shooting flow in laboratory experiments. *J. Sed. Petrol.*, **36**, 821–825.

Kenedi, C.L., **Sparks, R.S.J.**, **Malin, P.**, **Voight, B.**, **Dean, S.**, **Minshull, T.**, **Paulatto, M.**, **Peirce, C.** and **Shalev, E.** (2010) Contrasts in morphology and deformation offshore Montserrat: new insights from the SEA-CALIPSO marine cruise data. *Geophys. Res. Lett.*, **37**, 1–7.

Kennedy, J.F. (1961) *Stationary Waves and Antidunes in Alluvial Channels*. Report no. K11-R-2. W.M. Keck Laboratory of Hydraulics and Water Resources, California Institute of Technology, Pasadena, CA, 146 pp.

Kennedy, J.F. (1963) The mechanics of dunes and antidunes in erodible-bed channels. *J. Fluid Mech.*, **16**, 521–546.

Khezri, N. and **Chanson, H.** (2012a) Undular and breaking bores on fixed and movable gravel beds. *J. Hydraul. Res.*, **50**, 353–363.

Khezri, N. and **Chanson, H.** (2012b) Sediment inception under breaking tidal bores. *Mech. Res. Commun.*, **41**, 49–53.

Kjaer, K.H., **Sultan, L.**, **Krüger, J.** and **Schomaker, A.** (2004) Architecture and sedimentation of outwash fans in front of the Mýrdalsjfkull ice cap, Iceland. *Sed. Geol.*, **172**, 139–163.

Komar, P. (1987) Selective gravel entrainment and the empirical evaluation of flow competence. *Sedimentology*, **34**, 1165–1176.

Lang, J. and **Winesmann, J.** (2013) Lateral and vertical facies relationships of bedforms deposited by aggrading supercritical flows: from cyclic steps to humpback dunes. *Sed. Geol.*, **296**, 36–45.

Langford, R. and **Bracken, B.** (1987) Medano Creek, Colorado, A model for upper-flow-regime fluvial deposition. *J. Sed. Res.*, **57**, 863–870.

Laronne, J.B. and **Carson, M.A.** (1976) Interrelationships between bed morphology and bed-material transport for a small, gravel-bed channel. *Sedimentology*, **23**, 67–85.

Leclair, S.F., **Bridge, J.S.** and **Wang, F.** (1997) Preservation of cross-strata due to migration of subaqueous dunes over aggrading and non-aggrading beds: comparison of experimental data with theory. *Geosci. Can.*, **24**, 55–66.

Maejima, W., **Hota, R.N.** and **Mishra, B.** (2009) Antidunes and antidune stratification in the Permo-Carboniferous Talchir Formation, Talchir Gondwana Basin, Orissa, India. *J. Geosci.*, **52**, 11–20.

Magnússon, E., **Gudmundsson, M.T.**, **Roberts, M.J.**, **Sigurðsson, G.**, **Höskuldsson, F.** and **Oddsson, B.** (2012) Ice-volcano interactions during the 2010 Eyjafjallajökull eruption, as revealed by airborne imaging radar. *J. Geophys. Res.*, **117**, B07405. https://doi.org/10.1029/2012JB009250.

Marren, P.M., **Russell, A.J.** and **Rushmer, L.** (2009) Sedimentology of a sandur formed by multiple jökulhlaups, Kverkfjöll, Iceland. *Sed. Geol.*, **213**, 77–88.

Mather, A.E. and **Hartley, A.** (2005) Flow events on a hyper-arid alluvial fan: Quebrada Tambores, Salar de Atacama, northern Chile. In: *Alluvial Fans: Geomorphology, Sedimentology, Dynamics* (Eds A.M. Harvey, A.E. Mather and M. Stokes), *Geol. Soc. London Spec. Publ.*, **251**, 9–29.

Matthews, A.J., **Barclay, J.**, **Carn, S.**, **Thompson, G.**, **Alexander, J.**, **Herd, R.** and **Williams, C.** (2002) Rainfall-induced volcanic activity on Montserrat. *Geophys. Res. Lett.*, **29**, 22-1–22-4.

McBride, E.F., **Shepard, R.G.** and **Crawley, R.A.** (1975) Origin of parallel, near-horizontal laminae by

migration of bed forms in a small flume. *J. Sed. Petrol.*, **45**, 132–139.

Meirovich, L., **Laronne, J.B.** and **Reid, I.** (1998) The variation of water-surface slope and its significance for bedload transport during floods in gravel-bed streams. *J. Hydraul. Res.*, **36**, 147–157.

Middleton, G. (1965) Antidune cross-bedding in a large flume. *J. Sed. Petrol.*, **35**, 922–927.

Núñez-González, F. and **Martín-Vide, J.P.** (2011) Analysis of antidune migration direction. *J. Geophys. Res. Earth Surf.*, **116**, 1–16.

Parker, C., **Clifford, N.J.** and **Thorne, C.R.** (2011) Understanding the influence of slope on the threshold of coarse grain motion: revisiting critical stream power. *Geomorphology*, **126**, 51–65.

Petit, F., **Gob, F.**, **Houbrechts, G.** and **Assani, A.A.** (2005) Critical specific stream power in gravel-bed rivers. *Geomorphology*, **69**, 92–101.

Pierson, T.C. and **Scott, K.M.** (1985) Downstream dilution of a Lahar: transition from debris flow to a hyperconcentrated streamflow. *Water Resour. Res.*, **21**, 1511–1524.

Reid, I. and **Frostick, L.E.** (1987) Flow dynamics and suspended sediment properties in arid zone flash floods. *Hydrol. Process.*, **1**, 239–253.

SAC (2011) *Report to the Scientific Advisory Committee on Volcanic Activity at Soufrière Hills Volcano, Montserrat*. Report between 28 February 2010 and 31 October 2010. Open File Report OFR 10-02a.

Shaw, J. and **Kellerhals, R.** (1977) Paleohydraulic Interpretation of antidune bedforms with applications to antidunes in gravel. *J. Sed. Petrol.*, **47**, 257–266.

Shvidchenko, A.B. and **Pender, G.** (2000) Flume study of the effect of relative depth on the incipient motion of coarse uniform sediments. *Water Resour. Res.*, **36**, 619–628.

Stokes, M., **Griffiths, J.S.** and **Mather, A.** (2012) Palaeoflood estimates of Pleistocene coarse grained river terrace landforms (Río Almanzora, SE Spain). *Geomorphology*, **149–150**, 11–26.

Sušnik, J. (2009) *Lahars in the Belham River Valley, Montserrat, West Indies*. PhD Thesis. University of East Anglia, UK, 314 pp.

Tinkler, K.L. (1997a) Critical flow in rockbed streams with estimated values for Manning's *n*. *Geomorphology*, **20**, 147–164.

Tinkler, K.L. (1997b) Indirect velocity measurement from standing waves in rockbed rivers. *J. Hydraul. Eng.*, **123**, 918–921.

Vesipa, R., **Camporeale, C.**, **Ridolfi, L.** and **Chomaz, J.M.** (2014) On the convective-absolute nature of river bedform instabilities. *Phys. Fluids*, **26**, 1–15.

Wadge, G. (2000) *A DEM of the volcanic deposits of Soufrière Hills volcano during 1999*, Open File Report 00-07-1999, Montserrat Volcano Observatory

Wadge, G., **Voight, B.**, **Sparks, R.S.J.**, **Cole, P.D.**, **Loughlin, S.C.** and **Robertson, R.E.A.** (2014) Chapter 1 An overview of the eruption of Soufrière Hills Volcano, Montserrat from 2000 to 2010. In: *Eruption of Soufriere Hills Volcano, Montserrat from 2000 to 2010* (Eds G. Wadge, R.E.A. Robertson and B. Voight), Geological Society, London, Memoir, **39**, 1–40.

Yagishita, K. and **Taira, A.** (1989) Grain fabric of a laboratory antidune. *Sedimentology*, **36**, 1001–1005.

Yokokawa, M., **Masunda, F.**, **Sakai, T.**, **Endo, N.** and **Kubo, J.** (1999) Sedimentary structures and grain fabric of antidune cross-stratification in an experimental flume with sediment supply: Antidune cross-stratification (HCS mimics) in a flume. In: Proceedings of an International Workshop on Sediment Transport and Storage on Coastal Sea-Ocean System (Tsukuba, Japan), STA (JIS-TEC) & Geological Survey Japan, Tsukuba, pp. 409–414.

Yokokawa, M., **Hasegawa, K.**, **Kanbayashi, S.** and **Endo, N.** (2010) Formative conditions and sedimentary structures of sandy 3D antidunes: an application of the gravel step-pool model to fine-grained sand in an experimental flume. *Earth Surf. Proc. Land.*, **35**, 1720–1729.

Young, R.P., ed. (2008) *A Biodiversity Assessment of the Centre Hills, Montserrat*, Durrell Conservation Monograph No. 1, Durrell Wildlife Conservation Trust, Jersey, Channel Islands, 319 pp.

Zobin, V.M., **Plascencia, I.**, **Reyes, G.** and **Navarro, C.** (2009) The characteristics of seismic signals produced by lahars and pyroclastic flows: Volcán de Colima, México. *J. Volcanol. Geoth. Res.*, **179**, 157–167.

Manuscript received 12 December 2016; revision accepted 31 March 2017

Supporting Information

Additional Supporting Information may be found in the online version of this article:

Video Clip S1. Water-surface waves migrating upstream and individual wave breaking (Fig. 3C) from 18:06:40 to 18:07:27 UTC on 13/10/2012.

Video Clip S2. Water-surface waves breaking sequentially, the breaking of one individual wave in the train triggering the breaking of adjacent waves (Fig. 3C) from 18:06:40 to 18:07:27 UTC on 13/10/2012.

Video Clip S3. Water-surface wave train observed at site B1 (Fig. 3C) at 17:15 UTC on 14/12/2012.

Video Clip S4. Water-surface wave train observed at site B1 (Fig. 3C) at 17:30 UTC on 14/12/2012.

Video Clip S5. Downstream propagating, channel-wide turbulent surge (bore) (Fig. 3C) from 16:53:30 to 16:54:56 UTC on 13/10/2012.